

VARIATIONAL INFERENCE FORMULATION FOR A MODEL-FREE SIMULATION OF A DYNAMICAL SYSTEM WITH UNKNOWN PARAMETERS BY A RECURRENT NEURAL NETWORK

KYONGMIN YEO*, DYLAN E. C. GRULLON†, FAN-KENG SUN†, DUANE S. BONING†,
AND JAYANT R. KALAGNANAM*

Abstract. We propose a recurrent neural network for a “model-free” simulation of a dynamical system with unknown parameters without prior knowledge. The deep learning model aims to jointly learn the nonlinear time marching operator and the effects of the unknown parameters from a time series dataset. We assume that the time series data set consists of an ensemble of trajectories for a range of the parameters. The learning task is formulated as a statistical inference problem by considering the unknown parameters as random variables. A variational inference method is employed to train a recurrent neural network jointly with a feedforward neural network for an approximately posterior distribution. The approximate posterior distribution makes an inference on a trajectory to identify the effects of the unknown parameters and a recurrent neural network makes a prediction by using the outcome of the inference. In the numerical experiments, it is shown that the proposed variational inference model makes a more accurate simulation compared to the standard recurrent neural networks. It is found that the proposed deep learning model is capable of correctly identifying the dimensions of the random parameters and learning a representation of complex time series data.

Key word. Variational inference, Recurrent neural network, Dynamical system, Uncertainty quantification, Deep learning, Representation learning

AMS subject classifications. 37M05, 37M10, 62M45, 65C20

1. Introduction. Dynamical systems have been widely used in the modeling of complex physical, biological, and engineering processes [15, 36, 39]. Most of the dynamical systems have a few parameters that have to be identified either by a theoretical analysis or experiments [32, 41]. However, because of the high complexity of the physical (biological) systems, noise in the experimental data, and unresolved dynamics, it is very challenging to correctly identify those parameters, which introduces an uncertainty. Quantifying the effects of uncertainty in the simulation of a dynamical system has been extensively studied over the last two decades [14, 29, 42]. While most of the uncertainty quantification methods require almost complete knowledge on the system dynamics, such as the time marching operator and the source or distribution of the uncertainty, it is not uncommon, particularly in real-world applications, to encounter a very complex system, of which dynamics is not well understood.

“Model-free” approaches, which aim to identify the system dynamics from data, have been a long-standing research topic across many disciplines, *e.g.*, statistics, physics, engineering, and so on. Classical statistical models based on autoregressive stochastic processes or state-space models [5, 20] assume a linear transition of a state space to make an inference analytically tractable. Although nonlinear extensions of the classical methods have been widely used [1, 11], most of the nonlinear methods require at least partial knowledge on the system dynamics [18]. There has been a progress in the data-driven modeling of nonlinear dynamical systems based on a delay-coordinate embedding [19, 37]. A new class of methods, employing the dynamic mode decomposition supplemented with machine learning approaches, has been proposed to learn the governing equations directly from the data [7, 40]. Yet,

*IBM T.J. Watson Research Center, Yorktown Heights, NY, USA (kyeo@us.ibm.com).

†Department of Electrical Engineering and Computer Science, Massachusetts Institute of Technology, Cambridge, MA, USA

purely data-driven modeling of nonlinear dynamical systems remains as a challenging problem.

Recently, there has been a surge of interest in adopting deep learning techniques in the modeling of physical systems [6]. Due to its strength in learning nonlinear structures of the data, deep learning offers a powerful tool to build a computationally efficient and accurate surrogate model for the uncertainty quantification of physical systems [47]. The physics informed neural network (PINN) proposed by [30] uses the governing equations to impose a physical constraint in the training of an artificial neural network (ANN), which makes it possible to train an ANN with a sparse data. The new approach has inspired numerous follow-up studies, extending the framework to tackle the uncertainty quantification problems [16, 38, 43]. Although the initial results of PINN look promising [31], it requires a set of governing equations to impose physical constraints. For data-driven identification of nonlinear dynamical systems, [27] proposed a novel deep learning framework to learn a linear embedding of nonlinear dynamics based on the Koopman operator theory. [33] has proposed a feedforward neural network to learn the nonlinear time marching operator and a measurement noise, which employs a Runge-Kutta time integration scheme. [45] has proposed a recurrent neural network model, which is capable of approximating the probability distribution of a stochastic process without any distributional assumptions.

In a data-driven modeling, it is typically assumed that the data is acquired from one source, or under an identical condition. However, in practice, many of the dataset consist of an ensemble over a range of parameters. For examples, an experimental data consists of many sets of experiments with varying parameters, and a real-world observation data may be affected by changes in the environmental conditions. In general, it is very challenging to separate the effects of each parameter in the dynamics without knowing a functional relation even without a noise in the data due to complex nonlinear interactions. Data-driven identification of the effects of parameters can be thought as a representation learning problem, which has been of great interest in the data mining community [2]. In representation learning, we aim to find a low-dimensional representation from a complex data. In the context of the dynamical systems, if we can successfully find such a “representation” of the effects of the parameters from a dataset, the learned representation can be used to constrain the data-driven simulation to follow the correct dynamics. Built upon the recent advancement in a variational inference technique [24], a promising approach have been proposed [22, 46], where two neural networks are jointly trained to “disentangle” a time-invariant factor from a time-dependent feature.

In this study, we are interested in learning the time marching operator of a dynamical system from noisy observations, when the dataset consists of an ensemble of trajectories generated from a wide range of parameters. We formulate the learning task as a variational inference problem. It is shown that the proposed deep learning approach can identify the dimensionality of the parameters and make a more accurate simulation by exploiting the learned representation. This paper is organized as follows. A formal description of the problem setup is given in section 2.1. Section 2.2 describes the variational inference techniques and a probabilistic model is proposed to learn the nonlinear dynamics with unknown parameters. In section 3, the proposed model is tested against three nonlinear time series. Finally, the conclusions are given in section 4.

2. Methodology.

2.1. Problem formulation. Let $\boldsymbol{\mu} \in \mathbb{R}^d$ be the state of a physical system. The dynamics of $\boldsymbol{\mu}$ is governed by a system of differential equations;

$$(2.1) \quad \frac{d\boldsymbol{\mu}}{dt} = \mathcal{F}(\boldsymbol{\mu}, \mathbf{u}; \boldsymbol{\alpha}),$$

in which $\mathbf{u} \in \mathbb{R}^{N_u}$ is an exogenous forcing and $\boldsymbol{\alpha} \in \mathbb{R}^{N_\alpha}$ denotes the parameters of the governing equations. The exogenous forcing may come from an ambient condition, such humidity, temperature, and pressure, or a driving force, for example, electromagnetic field or pressure gradient. We do not assume a prior knowledge on the time marching operator, $\mathcal{F}(\cdot; \boldsymbol{\alpha})$. In general, the ground truth, $\boldsymbol{\mu}(t)$, is not accessible. We only observe a corrupted measurement, \mathbf{y}_t , at a discrete time interval, i.e.,

$$(2.2) \quad \mathbf{y}_t = \boldsymbol{\mu}_t + \boldsymbol{\epsilon}_t,$$

where $\mu_j = \mu(j\delta t)$, δt is a sampling interval, and $\boldsymbol{\epsilon}_t$ is a stochastic noise process. The time series data set consists of K trajectories of the noisy observations and exogenous forcing; $\mathcal{D} = \{(\mathbf{Y}_{0:T}^k, \mathbf{U}_{0:T}^k); k = 1, \dots, K\}$, where $\mathbf{Y}_{0:T}^k = (\mathbf{y}_0^k, \dots, \mathbf{y}_T^k)$ and $\mathbf{U}_{0:T}^k = (\mathbf{u}_0^k, \dots, \mathbf{u}_T^k)$. We assume that \mathcal{D} is generated by gathering data from the systems under a range of environmental conditions.

Here, we aim to build a data-driven model for the dynamics from an ensemble of the systems in (2.1), where the physical parameter, $\boldsymbol{\alpha}$, changes from one trajectory to another. To account for the variability of $\boldsymbol{\alpha}$, we consider $\boldsymbol{\alpha}$ as a random variable with a probability distribution, $p(\boldsymbol{\alpha})$. A trajectory in \mathcal{D} is assumed to be one realization from $p(\boldsymbol{\alpha})$, i.e.,

$$(2.3) \quad \frac{d\boldsymbol{\mu}^k}{dt} = \mathcal{F}(\boldsymbol{\mu}^k, \mathbf{u}^k; \boldsymbol{\alpha}^k), \quad \boldsymbol{\alpha}^k \sim p(\boldsymbol{\alpha}), \quad \text{for } k = 1, \dots, K,$$

and $\mathbf{y}_t^k = \boldsymbol{\mu}_t^k + \boldsymbol{\epsilon}_t^k$. Note that both \mathbf{u} and $\boldsymbol{\alpha}$ varies from one trajectory to another, while the random parameter, $\boldsymbol{\alpha}$, does not change over time. Further, we do not assume a prior knowledge on $p(\boldsymbol{\alpha})$.

The data generating distribution for \mathcal{D} is

$$(2.4) \quad \mathcal{D} \sim p(\mathbf{Y}_{0:T}, \boldsymbol{\alpha} | \mathbf{U}_{0:T}) = p(\mathbf{Y}_{0:T} | \boldsymbol{\alpha}, \mathbf{U}_{0:T}) p(\boldsymbol{\alpha}),$$

Without a prior knowledge on $\mathcal{F}(\cdot; \boldsymbol{\alpha})$, even the dimensionality of $\boldsymbol{\alpha}$ is not known, which makes it challenging to directly model the data generating distribution (2.4). To circumvent the difficulties, we introduce a latent variable, $\mathbf{z} \in \mathbb{R}^{N_z}$, and aim to learn a probabilistic model, such that

$$(2.5) \quad \mathcal{D} \sim p(\mathbf{Y}_{0:T} | \mathbf{U}_{0:T}, \mathbf{z}) p(\mathbf{z}).$$

Note the similarity between (2.4) and (2.5). In the probabilistic model, it is not of central interest to find the marginal distribution of \mathbf{z} . The major goal is to find an accurate time marching operator for \mathbf{y} ,

$$(2.6) \quad p(\mathbf{Y}_{0:T} | \mathbf{U}_{0:T}, \mathbf{z}) = \prod_{i=0}^{T-1} p(\mathbf{y}_{i+1} | \mathbf{y}_i, \mathbf{u}_i, \mathbf{z}).$$

Hence, there are two major tasks. The first task is to train an inference model for \mathbf{z} given a trajectory $(\mathbf{Y}_{0:T}, \mathbf{U}_{0:T}) \in \mathcal{D}$, i.e., $p(\mathbf{z} | \mathbf{Y}_{0:T}, \mathbf{U}_{0:T})$. Then, a generative model is trained with respect to the latent variable, i.e., $p(\mathbf{Y}_{0:T} | \mathbf{U}_{0:T}, \mathbf{z})$, in which $\mathbf{z} \sim p(\mathbf{z} | \mathbf{Y}_{0:T}, \mathbf{U}_{0:T})$. In this study, we employ a variational inference technique to jointly train the inference and generative models.

2.2. Variational Inference. Variational inference (VI) has been widely used in the Machine Learning community due to its strength in learning an inference model of a latent variable [4]. The original formulation of VI imposes some restrictions on the probabilistic model to make the inference problem analytically tractable [3]. Recently, [24] proposed a VI formulation for artificial neural networks. The new VI method allows more flexible probabilistic models by using artificial neural networks. In this study, we employ the VI formulation by [24].

In a variational inference, we aim to find an approximate posterior distribution of the latent variable, $q(\mathbf{z}|\mathbf{Y}_{0:T}, \mathbf{U}_{0:T})$, because the true posterior distribution, $p(\mathbf{z}|\mathbf{Y}_{0:T}, \mathbf{U}_{0:T})$, is intractable. Hereafter, we omit the obvious dependence on the exogenous forcing, $\mathbf{U}_{0:T}$, in the notation for simplicity. The marginal log likelihood function of \mathcal{D} can be written as

$$(2.7) \quad \sum_{i=1}^K \log p(\mathbf{Y}_{0:T}^i) = \sum_{i=1}^K D_{KL}(q(\mathbf{z}|\mathbf{Y}_{0:T}^i)||p(\mathbf{z}|\mathbf{Y}_{0:T}^i)) + \text{ELBO}.$$

Here, $D_{KL}(q||p)$ denotes the Kullback-Leibler divergence,

$$(2.8) \quad D_{KL}(q(\mathbf{z})||p(\mathbf{z})) = \int q(\mathbf{z}) \log \frac{q(\mathbf{z})}{p(\mathbf{z})} d\mathbf{z}.$$

The evidence lower bound (ELBO) is

$$(2.9) \quad \text{ELBO} = - \sum_{i=1}^K \left\{ D_{KL}(q(\mathbf{z}|\mathbf{Y}_{0:T}^i)||p(\mathbf{z})) - E_{\mathbf{z} \sim q(\mathbf{z}|\mathbf{Y}_{0:T}^i)} [\log p(\mathbf{Y}_{0:T}^i|\mathbf{z})] \right\},$$

in which $p(\mathbf{z})$ is a prior distribution. It is straightforward to prove (2.7) by expanding the terms on the right-hand side of (2.7) and applying Bayes' theorem,

$$p(\mathbf{Y}_{0:T}) = \frac{p(\mathbf{Y}_{0:T}|\mathbf{z})p(\mathbf{z})}{p(\mathbf{z}|\mathbf{Y}_{0:T})}.$$

The Kullback-Leibler divergence defines a distance between two probability distributions and is always non-negative. Hence, ELBO on the right-hand side of (2.7) provides a ‘‘lower bound’’ of the marginal log likelihood. Maximizing ELBO corresponds to minimizing the difference between the true and an approximate posterior distributions.

The second term in ELBO is computed by using a recurrent neural network (RNN), such as the Long Short-Term Memory Network or the Gated Recurrent Unit. A recurrent neural network is a nonlinear state-space model to tackle a sequential inference problem [17]. A recurrent neural network consists of two steps,

$$(2.10) \quad \mathbf{h}_{t+1} = \Psi_h(\mathbf{h}_t, \mathbf{y}_t, \mathbf{z}),$$

$$(2.11) \quad p(\mathbf{y}_{t+1}|\mathbf{h}_{t+1}) = \Psi_y(\mathbf{h}_{t+1}),$$

in which \mathbf{h}_t is a hidden state, and Ψ_h and Ψ_y are the nonlinear functions of the RNN. It is clearly shown that \mathbf{y}_{t+1} becomes conditionally independent from the past, $\mathbf{Y}_{0:t}$, given the hidden state, \mathbf{h}_{t+1} . From the conditional independence, the marginal likelihood function of a trajectory becomes

$$(2.12) \quad p(\mathbf{Y}_{0:T}|\mathbf{z}) = \int \cdots \int \left[\prod_{t=1}^T p(\mathbf{y}_t|\mathbf{h}_t)p(\mathbf{h}_t|\mathbf{h}_{t-1}, \mathbf{y}_{t-1}, \mathbf{z}) \right] p(\mathbf{y}_0)p(\mathbf{h}_0)d\mathbf{h}_0 \cdots d\mathbf{h}_T.$$

Due to the deterministic nature, the transition probability of RNN is given by a Dirac delta function,

$$(2.13) \quad p(\mathbf{h}_{t+1}|\mathbf{h}_t, \mathbf{y}_t, \mathbf{z}) = \delta(\mathbf{h}_{t+1} - \Psi_h(\mathbf{h}_t, \mathbf{y}_t, \mathbf{z})).$$

If we further assume the prior distribution, $p(\mathbf{h}_0) = \delta(\mathbf{0})$, the marginal likelihood function (2.12) becomes

$$(2.14) \quad p(\mathbf{Y}_{0:T}|\mathbf{z}) = \left[\prod_{t=1}^T p(\mathbf{y}_t|\mathbf{h}_t) \right] p(\mathbf{y}_0),$$

and, hence, the log likelihood function is simply

$$(2.15) \quad \log p(\mathbf{Y}_{0:T}|\mathbf{z}) = \sum_{t=1}^T \log p(\mathbf{y}_t|\mathbf{h}_t) + \log p(\mathbf{y}_0).$$

Note that \mathbf{h}_t is a function of the entire trajectory up to $t-1$, i.e., $\mathbf{Y}_{1:t-1}$, as well as the latent variable, \mathbf{z} . Here, we use a Gaussian distribution with a diagonal covariance as a probabilistic model for RNN,

$$(2.16) \quad p(\mathbf{y}_t|\mathbf{h}_t) = \mathcal{N}(\mathbf{y}_t; \boldsymbol{\mu}_t, \text{diag}(\boldsymbol{\sigma}_t^2)).$$

Here, $\boldsymbol{\mu}_t \in \mathbb{R}^d$ and $\boldsymbol{\sigma}_t \in \mathbb{R}^d$ are, respectively, the mean and standard deviation of the Gaussian distribution, and $\text{diag}(\cdot)$ denotes a diagonal matrix. The recurrent neural network, $\Psi = (\Psi_y \circ \Psi_h)$, takes $(\mathbf{y}_{t-1}, \mathbf{h}_{t-1}, \mathbf{z})$ as an input, and the output is a $\mathbb{R}^{d \times 2}$ matrix, which provides $\boldsymbol{\mu}_t$ and $\boldsymbol{\sigma}_t$;

$$(\boldsymbol{\mu}_t, \log \boldsymbol{\sigma}_t) = \Psi(\mathbf{y}_{t-1}, \mathbf{h}_{t-1}, \mathbf{z}).$$

Note that the artificial neural network computes $\log \sigma_t$, instead of σ_t , which makes it easier to satisfy the positivity constraint, $\sigma_t > 0$. Then, the log likelihood function (2.15) becomes

$$(2.17) \quad \log p(\mathbf{Y}_{1:T}|\mathbf{z}) = - \sum_{t=1}^T \sum_{i=1}^d \left\{ \frac{1}{2} \left(\frac{y_{ti} - \mu_{ti}}{\sigma_{ti}} \right)^2 + \log \sigma_{ti} \right\} + C.$$

Here, the constant terms are lumped together in C . Note that, if the probabilistic model for RNN is given as a Gaussian with a constant diagonal covariance, i.e., $\boldsymbol{\sigma}_t = \sigma$, and σ is not estimated, (2.17) reduces to the standard mean-square loss function, which is typically used in a standard RNN. Since (2.17) provides a measure about how well the time series data is reconstructed by RNN, it is called a ‘‘reconstruction error’’.

It is typical to minimize negative ELBO instead of maximizing ELBO. The loss function of the variational inference problem is

$$(2.18) \quad \mathcal{L} = \sum_{i=1}^K D_{KL}(q(\mathbf{z}|\mathbf{Y}_{0:T}^i)||p(\mathbf{z})) - E_{\mathbf{z} \sim q(\mathbf{z}|\mathbf{Y}_{0:T}^i)} \left[\sum_{t=1}^T \log p(\mathbf{y}_t^i|\mathbf{h}_t) \right].$$

An isotropic Gaussian distribution is used as the prior distribution,

$$p(\mathbf{z}) = \mathcal{N}(\mathbf{z}; \mathbf{0}, \sigma_z^2 \mathbf{I}).$$

Similar to the generative RNN model, we use a Gaussian distribution with a diagonal covariance for the posterior distribution;

$$q(\mathbf{z}|\mathbf{Y}_{0:T}) = \mathcal{N}(\mathbf{z}; \mathbf{m}_q, \text{diag}(\boldsymbol{\sigma}_q^2)),$$

where $\mathbf{m}_q \in \mathbb{R}^{N_z}$ and $\boldsymbol{\sigma}_q \in \mathbb{R}^{N_z}$ denote the mean and standard deviation, respectively. We use a feed-forward artificial neural network, $\boldsymbol{\eta}$, to approximate the posterior distribution, such that

$$(2.19) \quad (\mathbf{m}_q, \log \boldsymbol{\sigma}_q) = \boldsymbol{\eta}(\mathbf{Y}_{0:T}).$$

Again, the output of $\boldsymbol{\eta}$ is a $\mathbb{R}^{N_z \times 2}$ matrix, which provides \mathbf{m}_q and $\boldsymbol{\sigma}_q$. Then, the Kullback-Leibler divergence in ELBO can be computed analytically,

$$(2.20) \quad D_{KL}(q(\mathbf{z}|\mathbf{Y}_{0:T})||p(\mathbf{z})) = \sum_{i=1}^{N_z} \left\{ \frac{1}{2} \frac{\sigma_{q_i}^2 + m_{q_i}^2}{\sigma_z^2} - \log \left(\frac{\sigma_{q_i}}{\sigma_z} \right) \right\} - \frac{N_z}{2}.$$

After [9], it has become popular to use an artificial neural network for the prior distribution, $p(\mathbf{z})$, which is jointly trained with $q(\mathbf{z}|\mathbf{Y}_{0:T})$. However, as shown in [A](#), training the prior and posterior distributions jointly leads to an ill-posed problem and, thus, should be avoided. Finally, the loss function is

$$(2.21) \quad \mathcal{L}_q^k = \sum_{i=1}^{N_z} \left\{ \frac{1}{2} \frac{\sigma_{q_i}^2 + m_{q_i}^2}{\sigma_z^2} - \log \left(\frac{\sigma_{q_i}}{\sigma_z} \right) \right\} \Big|_{\mathbf{Y}_{0:T}^k}$$

$$(2.22) \quad \mathcal{L}_y^k = E_{\mathbf{z} \sim q(\mathbf{z}|\mathbf{Y}_{0:T}^k)} \left[\sum_{t=1}^T \sum_{i=1}^d \frac{1}{2} \frac{(y_{t_i}^k - \mu_{t_i})^2}{\sigma_{t_i}^2} + \log \sigma_{t_i} \right],$$

$$(2.23) \quad \mathcal{L} = \sum_{k=1}^K (\mathcal{L}_q^k + \mathcal{L}_y^k) + C.$$

Again, all the constant terms are lumped together in C .

The first term in the loss function (2.23) plays a role of a regularization to keep $q(\mathbf{z}|\mathbf{Y}_{0:T})$ around $p(\mathbf{z})$, while the second term tries to move $q(\mathbf{z}|\mathbf{Y}_{0:T})$ away from $p(\mathbf{z})$ in the direction of minimizing the reconstruction. The loss function has a similar structure with a standard regularized optimization problem, but without an explicit regularization coefficient. Note, however, that \mathcal{L}_y depends on the length of the time series, T . If we limit our interest to a stationary, or ergodic, system, the distribution of the reconstruction error per one time step is also stationary,

$$\langle \log p(\mathbf{y}_t|\mathbf{h}_t) \rangle = \dots = \langle \log p(\mathbf{y}_{t+T}|\mathbf{h}_{t+T}) \rangle,$$

where $\langle \cdot \rangle$ denotes an ensemble average. Then, the loss function can be written as

$$\mathcal{L}_y = -E_{\mathbf{z} \sim q(\mathbf{z}|\mathbf{Y}_{0:T})} [\log p(\mathbf{Y}_{0:T}|\mathbf{z})] \simeq -T \cdot E_{\mathbf{z} \sim q(\mathbf{z}|\mathbf{Y}_{0:T})} [\langle \log p(\mathbf{y}_t|\mathbf{h}_t) \rangle].$$

Now, it is obvious that \mathcal{L}_y increases linearly with T , while \mathcal{L}_q is fixed. So, for a larger T , the relative contribution of \mathcal{L}_q to \mathcal{L} becomes smaller, which makes the effects of the regularization (Kullback-Leibler divergence) weaker. Hence, the length of a time series, T , implicitly plays a role of a regularization coefficient. In fact, T is a free parameter that one has to choose when training a RNN. For a standard RNN, T is

chosen to be larger than a characteristic time scale of the process, but short enough to have the training computationally tractable.

Let T_{ref} be the length of a time series for an optimal regularization, and T be the length of the time series chosen for a proper training of the RNN. When $T_{ref} \gg T$, due to the stationarity of the reconstruction error, it is unnecessary to compute the RNN for T_{ref} . Instead, we only need to rescale the loss function, such that

$$(2.24) \quad \mathcal{L} = \sum_{k=1}^K \left(\mathcal{L}_q^k + \frac{T_{ref}}{T} \mathcal{L}_y^k \right) + C = \frac{T_{ref}}{T} \sum_{k=1}^K (\lambda \mathcal{L}_q^k + \mathcal{L}_y^k) + C,$$

in which $\lambda = T/T_{ref}$. Since the scaling factor and the constant term are irrelevant in optimization, we can define a new loss function as

$$(2.25) \quad \mathcal{L} = \sum_{k=1}^K \lambda \mathcal{L}_q^k + \mathcal{L}_y^k.$$

Note that (2.25) has a similar structure with β -VAE (variational auto-encoder) proposed by [21]. While they derived β -VAE from a constrained optimization formulation, here we show that the same formulation naturally arises from a variational inference method for a time series problem.

In most of the current deep learning frameworks, such as TensorFlow and PyTorch, once the network and loss functions are defined, the computational graph is automatically constructed and the gradients of the loss function with respect to the network parameters can be automatically computed, which makes it easy to train a deep learning model without understanding the mathematical details. Nevertheless, we provide a more detailed explanation about the model training in B.

2.3. Artificial Neural Network. The recurrent neural network used in this study consists of three layers. The first layer transforms the input variable,

$$(2.26) \quad \Psi_x = (\mathcal{R} \circ \mathbf{L}^{N_c})(\mathbf{x}_t).$$

Here, $\mathbf{x}_t \in \mathbb{R}^{N_x}$ is the input variable, N_c is the number of neurons in the RNN, $\mathbf{L}^a(\mathbf{x})$ is a linear transformation,

$$\mathbf{L}^a = \mathbf{W}\mathbf{x} + \mathbf{b},$$

in which $\mathbf{W} \in \mathbb{R}^{a \times N_x}$ and $\mathbf{b} \in \mathbb{R}^a$ denote the weight matrix and bias vector, respectively, and $\mathcal{R}(\cdot)$ is a linear rectifier,

$$\mathcal{R}(x) = \max(0, x).$$

In the variational inference problem, the input variable is $\mathbf{x}_t^T = (\mathbf{y}_t^T, \mathbf{z}^T)^T$ and, for a standard RNN, $\mathbf{x}_t = \mathbf{y}_t$. We use a two-level Gated Recurrent Units (GRU) for the second layer to compute the time evolution of the state variables [8],

$$(2.27) \quad \mathbf{h}_{t+1}^{(1)} = \text{GRU}_1(\mathbf{h}_t^{(1)}, \Psi_x),$$

$$(2.28) \quad \mathbf{h}_{t+1}^{(2)} = \text{GRU}_2(\mathbf{h}_t^{(2)}, \mathbf{h}_{t+1}^{(1)}).$$

Here, $\mathbf{h}_t^{(1)}$ and $\mathbf{h}_t^{(2)}$ denote the internal states of GRU_1 and GRU_2 , respectively. Finally, the last layer computes the mapping between the state vector and the generative

distribution,

$$(2.29) \quad \mathbf{g} = (\mathcal{R} \circ \mathbf{L}_g^{N_g})(\mathbf{h}_{t+1}^{(2)})$$

$$(2.30) \quad \boldsymbol{\mu}_{t+1} = \mathbf{L}_\mu^d(\mathbf{g}), \quad \log(\boldsymbol{\sigma}_{t+1}) = \mathbf{L}_\sigma^d(\mathbf{g}).$$

In the numerical experiments for the dynamical systems considered in this study, the difference between LSTM and GRU is not noticeable, while GRU has a smaller number of parameters. For more complex problems, however, LSTM may outperform our RNN model due to the large number of parameters [13].

The approximate posterior distribution, $q(\mathbf{z}|\mathbf{Y}_{0:T})$, has an explicit dependence on the length of the sequence used in the training, *i.e.*, $\boldsymbol{\eta}(\mathbf{Y}_{0:T})$. Because the length of the training sequence, T , is nothing but a free parameter we choose to facilitate the training, it is undesirable to have $\boldsymbol{\eta}$ fixed to T . Note that the purpose of $q(\mathbf{z}|\mathbf{Y}_{0:T})$ is to identify the correct latent state that can explain the dynamics observed in the conditioning sequence, $\mathbf{Y}_{0:T}$. Hence, as long as the length of the conditioning sequence is longer than a characteristic timescale of the process, it is desirable to have $\boldsymbol{\eta}$ adaptable to any sequence length.

To develop a more flexible model, we propose to use a pre-trained RNN to provide the conditioning variable to $q(\mathbf{z}|\mathbf{Y}_{0:T})$. Let Ψ_h^{pre} be a pre-trained RNN, *e.g.*, the first two layer of the RNN defined above, (2.26 – 2.28). Ψ_h^{pre} may be trained as a standard RNN for the entire data set, \mathcal{D} . From the state-space model description of RNN, it is clear that [17],

$$(2.31) \quad \begin{aligned} \mathbf{h}_{t+1}^{pre} &= \Psi_h^{pre}(\mathbf{y}_t, \Psi_h^{pre}(\mathbf{y}_{t-1}, \Psi_h^{pre}(\dots \Psi_h^{pre}(\mathbf{y}_1, \Psi_h^{pre}(\mathbf{y}_0, \mathbf{h}_0)) \dots)) \\ &= f(\mathbf{y}_t, \dots, \mathbf{y}_0, \mathbf{h}_0). \end{aligned}$$

Here, $\mathbf{h}_t^{pre} = (\mathbf{h}_t^{(1)}, \mathbf{h}_t^{(2)})$. It is shown that the hidden state, \mathbf{h}_{t+1}^{pre} , provides a representation of $\mathbf{Y}_{0:t}$. Because Ψ_h approximates a relaxation process [45], the dependence on \mathbf{h}_0 will vanish when t is larger than a relaxation timescale.

Now, let define an artificial neural network for the approximate posterior as

$$(2.32) \quad \boldsymbol{\eta} = (\hat{\boldsymbol{\eta}} \circ \Psi_{h,t}^{pre})(\mathbf{Y}_{0:t}).$$

Here, $\Psi_{h,t}^{pre}$ indicates computing the pre-trained RNN over an input sequence, $\mathbf{Y}_{0:t}$, to compute \mathbf{h}_{t+1}^{pre} . The artificial neural network, $\hat{\boldsymbol{\eta}}$, consists of the following operations,

$$(2.33) \quad \mathbf{v}_i = (\mathcal{R} \circ \mathbf{L}_{v_i}^{N_{v_i}})(\mathbf{v}_{i-1}), \text{ for } i = 1, \dots, N_\eta,$$

$$(2.34) \quad \mathbf{m}_q = \mathbf{L}_m^{N_z}(\mathbf{v}_{N_\eta}), \quad \log(\boldsymbol{\sigma}_q) = \mathbf{L}_{\sigma_q}^{N_z}(\mathbf{v}_{N_\eta}),$$

in which $\mathbf{v}_0 = \mathbf{h}_{t+1}^{pre}$, N_η is the number of the layers, and N_{v_i} is the number of neurons in each layer. In other words, $\hat{\boldsymbol{\eta}}$ is a multi-layer feedforward network.

In summary, the proposed variational inference model requires training two recurrent neural networks and one feedforward neural network;

$$(2.35) \quad p(\mathbf{y}_t|\mathbf{Y}_{0:t-1}) = (\Psi_y^{pre} \circ \Psi_h^{pre})(\mathbf{y}_{t-1}, \mathbf{h}_{t-1}^{pre}) \text{ for } t = 1, \dots, T,$$

$$(2.36) \quad q(\mathbf{z}|\mathbf{Y}_{0:T}) = (\hat{\boldsymbol{\eta}} \circ \Psi_{h,T}^{pre})(\mathbf{Y}_{0:T}),$$

$$(2.37) \quad p(\mathbf{y}_t|\mathbf{Y}_{0:t-1}, \mathbf{z}) = (\Psi_y^{VI} \circ \Psi_h^{VI})(\mathbf{y}_{t-1}, \mathbf{h}_{t-1}, \mathbf{z}) \text{ for } t = 1, \dots, T.$$

Here, the first RNN (2.35) is trained independently by using the standard back-propagation through time method. Once Ψ_h^{pre} is obtained, the VI models (2.36–2.37) are jointly trained as explained in B.

2.4. Simulation Method. Once the inference and generative models are trained, a stochastic simulation can be performed to compute the time evolution of the probability density function [45]. For a one-step-ahead prediction, *i.e.*, computing the probability distribution at $T + 1$ given the data up to T , we need to compute

$$(2.38) \quad p(\mathbf{y}_{T+1}|\mathbf{Y}_{0:T}, \mathbf{U}_{0:T}) = \int p(\mathbf{y}_{T+1}|\mathbf{Y}_{-\tau:T}, \mathbf{U}_{-\tau:T}, \mathbf{z})q(\mathbf{z}|\mathbf{Y}_{-\tau:0}, \mathbf{U}_{-\tau:0})d\mathbf{z}.$$

Note that it requires a ‘‘spin-up’’ period, $t \in [-\tau, 0]$, to initialize the simulation. The spin-up period is required not only to identify the effects of the unknown parameters by $q(\mathbf{z})$, but also to remove the spurious effects from the misspecification of the initial condition of a RNN. Due to the lack of a physical meaning of the hidden state of a RNN, \mathbf{h}_t , we have no choice but to start a simulation from an arbitrary value, usually zero, for \mathbf{h}_0 . The integration over the approximate posterior distribution is computed by using a Monte Carlo method. We first compute, $q(\mathbf{z}|\mathbf{Y}_{-\tau:0}, \mathbf{U}_{-\tau:0})$, and draw M samples;

$$\mathbf{z}^{(m)} \sim q(\mathbf{z}|\mathbf{Y}_{-\tau:0}, \mathbf{U}_{-\tau:0}) \quad \text{for } m = 1, \dots, M.$$

Then, M recurrent neural networks (Ψ^{VI}) are run through the dataset with the input sequence, $x_{t-1}^{(m)} = (y_{t-1}, \mathbf{z}^{(m)})$ for $t = -\tau, \dots, T$ and $m = 1, \dots, M$ to evaluate $p(y_{T+1}|\mathbf{Y}_{-\tau:T}, \mathbf{U}_{-\tau:T}, \mathbf{z}^{(m)})$. Finally, the predictive distribution is approximated by a mixture distribution,

$$(2.39) \quad \mu_{T+1} = \frac{1}{M} \sum_{m=1}^M \mu_{T+1}^{(m)},$$

$$(2.40) \quad \sigma_{T+1}^2 = \frac{1}{M} \sum_{m=1}^M \mu_{T+1}^{(m)2} + \sigma_{T+1}^{(m)2} - \mu_{T+1}^2,$$

$$(2.41) \quad p(y_{T+1}|\mathbf{Y}_{-\tau:T}, \mathbf{U}_{-\tau:T}) = \mathcal{N}(\mu_{T+1}, \sigma_{T+1}^2),$$

in which $\mu_{T+1}^{(m)}$ and $\sigma_{T+1}^{(m)}$ denote the outputs of Ψ^{VI} for $x_T^{(m)}$.

A multiple-step prediction corresponds to computing the time evolution of the probability density function due to the nonlinear marching operator. Unlike the one-step-ahead prediction, a multiple-step prediction requires to marginalize over \mathbf{z} as well as all the intermediate time steps, *i.e.*;

(2.42)

$$p(\mathbf{y}_{T+1}|\mathbf{Y}_{-\tau:0}, \mathbf{U}_{-\tau:T}) = E_{\mathbf{z} \sim q(\mathbf{z}|\mathbf{Y}_{-\tau:0})} \left[\int \prod_{t=1}^T p(\mathbf{y}_{t+1}|\mathbf{Y}_{-\tau:t}, \mathbf{U}_{-\tau:t}, \mathbf{z})p(\mathbf{y}_1|\mathbf{Y}_{-\tau:0}, \mathbf{U}_{-\tau:0}, \mathbf{z})d\mathbf{y}_t \right], \quad \text{for } T \geq 1.$$

Note that \mathbf{U} is assumed to be given for the simulation. In C, a Monte Carlo simulation procedure is outlined.

3. Numerical experiments. In the numerical experiments, the dimension of the internal state of the RNN is fixed at $N_c = 128$ both for the conditioning RNN (Ψ^{pre}) and the decoder RNN (Ψ^{VI}). Hence, the only difference between Ψ^{pre} and Ψ^{VI} is the number of input variables in (2.26). For Ψ^{pre} , $\mathbf{x}_t = (\mathbf{y}_t, \mathbf{u}_t)$, while the input variable to Ψ^{VI} is $\mathbf{x}_t = (\mathbf{y}_t, \mathbf{u}_t, \mathbf{z})$. The posterior network ($\hat{\eta}$) is a three-layer

feedforward network and the number of neurons in each layer is equal to the dimension of \mathbf{h}^{pre} , i.e., $N_\eta = 3$ and $N_{v_i} = 2 \times N_c = 256$ for $i = 1, 2, 3$. The dimension of the latent variable is $N_z = 10$.

Both the conditioning RNN and the variational inference model ($\Psi^{VI} + \hat{\eta}$) are trained by using a minibatch stochastic gradient descent method, called ADAM [23]. The initial learning rate is set to $\xi_{max} = 10^{-3}$ and decreased by the following cosine function [26],

$$(3.1) \quad \xi_l = \xi_{min} + \frac{\xi_{max} - \xi_{min}}{2} \left\{ 1 + \cos \left(\frac{l}{L} \pi \right) \right\},$$

in which l is the iteration count. The minimum learning rate and the maximum number of iterations are set to $\xi_{min} = 10^{-4}$ and $L = 3 \times 10^4$, respectively. The momentum coefficients of ADAM are set to the default values recommended in [23]. The size of the minibatch is 20. At each SGD iteration, 20 training data are randomly selected from \mathcal{D} by first randomly sampling from the K trajectories *with replacement* and then randomly selecting the starting point of those trajectories. The length of the training sequence is set to 200 time steps. The size of the Monte Carlo samples to evaluate the loss function \mathcal{L}_y is 25.

In all of the experiments, the dataset consists of 500 trajectories, each with a length of 1,000 time steps, i.e., $K = 500$ and $T = 1,000$. The variables are normalized by the respective maximum and minimum values, e.g.,

$$y_i^* = \frac{y_i - \min(y_i)}{\max(y_i) - \min(y_i)} - 0.5, \text{ for } i = 1, \dots, d.$$

The dataset (\mathcal{D}) is separated into two disjoint datasets, one for the training and the other for the validation. The training dataset (\mathcal{D}_T) consists of the first 400 trajectories in \mathcal{D} and the rest 100 trajectories are in the validation dataset (\mathcal{D}_V).

3.1. Mackey-Glass Time Series. We first consider the Mackey-Glass time series with random parameters. The Mackey-Glass equation is a nonlinear time-delay dynamical system [28],

$$(3.2) \quad \frac{d\phi(t)}{dt} = \frac{\alpha\phi(t - \tau)}{1 + \phi^{10}(t - \tau)} - \gamma\phi(t).$$

The dynamics of the Mackey-Glass system switches between periodic and chaotic, depending on the set of parameters. The Mackey-Glass equation has been extensively used as a benchmark system to investigate time-delay dynamics [12, 35, 10].

To create the dataset, $\mathcal{D} = \{(y_0^k, \dots, y_T^k); k = 1, \dots, 500, T = 1000\}$, first, ground-truth trajectories are generated by randomly sampling the three parameters in (3.2) from uniform distributions,

$$(3.3) \quad \alpha \sim \mathcal{U}(0.2, 0.4), \quad \gamma \sim \mathcal{U}(0.05, 0.1), \quad \tau \sim \mathcal{U}(20, 40).$$

The parameters are chosen around an onset of a chaos regime [12]. Figure 1 shows four sample trajectories in the data set. The Mackey-Glass equation is integrated by using a third-order Adams-Bashforth method with the time-step size of 0.01. Then, the ground-truth trajectories are downsampled to make time series data with a sampling interval of $\delta t = 1$. Finally, the time series data is perturbed by an uncorrelated random noise,

$$(3.4) \quad y_t^k = \phi^k(t\delta t) + \epsilon_t^k, \text{ for } k = 1, \dots, 500 \text{ and } t = 1, \dots, 1000.$$

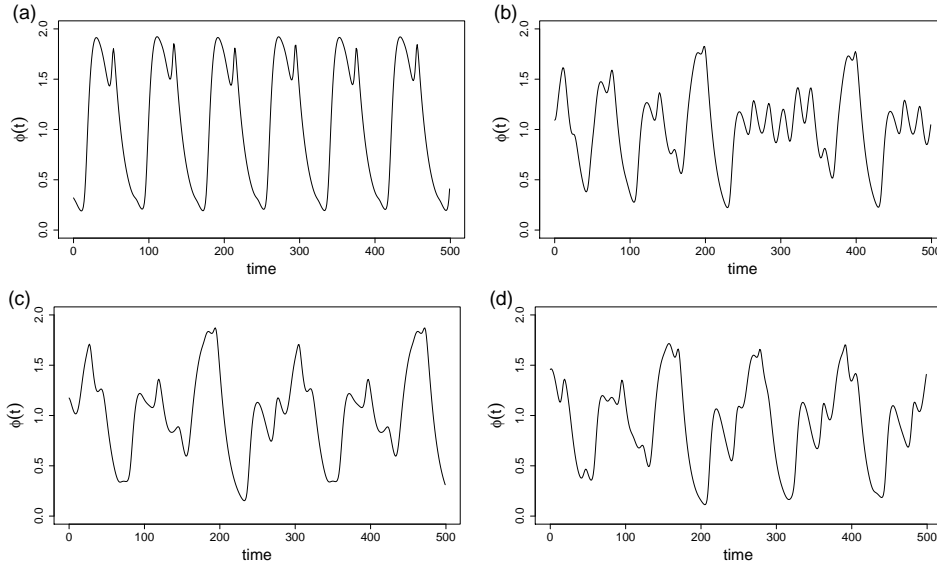


FIG. 1. Sample ground-truth trajectories of the Mackey-Glass time series for different sets of the parameters, (α, γ, τ) ; (a) $(0.350, 0.070, 33.72)$, (b) $(0.242, 0.080, 24.44)$, (c) $(0.222, 0.076, 31.79)$, (d) $(0.257, 0.094, 31.85)$.

TABLE 1
Normalized root mean-square error and log likelihood (NLL) of RNN and VI-RNN.

λ	RNN		VI-RNN		
	-	0.01	0.1	1.0	10.0
e_μ	0.030	0.028	0.028	0.026	0.031
NLL	0.975	0.976	0.977	0.981	0.972

Here, the noise process is $\epsilon_t^k \sim \mathcal{N}(0, \sigma_\epsilon^2)$. The standard deviation of ϵ is $\sigma_\epsilon = 0.03$, which is about 5% of the standard deviation of \mathcal{D} .

We first compare the performances of the proposed variational-inference problem (VI-RNN) and the standard RNN for an one-step-ahead prediction task, *i.e.*, sequentially making a prediction of (μ_t, σ_t) by using (y_0, \dots, y_{t-1}) . Hereafter, we use RNN to refer to the results from the standard RNN model, unless stated otherwise. The one-step-ahead prediction of VI-RNN is evaluated with $(M = 200)$ samples as outlined in section 2.4.

The model performance is evaluated against the 100 trajectories in \mathcal{D}_V . The length of the testing trajectory is $T = 600$. After the simulations are performed for $t = 1, \dots, 600$, the first 200 time steps are discarded and the error metrics are computed for $t = 201, \dots, 600$ to remove the data used for the conditioning of the latent variable, $q(\mathbf{z}|\mathbf{Y}_{0:200})$, from the evaluation. Two error metrics are considered. The normalized root mean-square error is defined with respect to the ground-truth;

$$(3.5) \quad e_\mu = \left[\frac{1}{|\mathcal{D}_V|} \sum_{k=1}^{|\mathcal{D}_V|} \overline{\frac{(\mu^k - \phi^k)^2}{\text{Var}(\phi^k)}} \right]^{1/2},$$

in which the overline denotes a time average over the length of the evaluation period,

$Var(\phi^k)$ is the variance of the k -th ground-truth times series, and $|\mathcal{D}_V|$ is the size of the validation dataset. The log likelihood (LL) is computed without the constant term,

$$(3.6) \quad LL = \frac{1}{|\mathcal{D}_V|} \sum_{k=1}^{|\mathcal{D}_V|} \frac{1}{2} \frac{(\mu^k - y^k)^2}{\sigma^k} - \log(\sigma^k).$$

Then, LL is normalized by that of a perfect model,

$$(3.7) \quad NLL = \frac{LL}{-0.5 - \log(\sigma_\epsilon)}.$$

The normalized log likelihood (NLL) provides a relative performance of the model with respect to a perfect inference model and is always less than one.

The two error metrics are shown in table 1. VI-RNNs are trained with four different penalty parameters, $\lambda = 0.01, 0.1, 1, 10$. It shows that, in general, VI-RNN makes better inferences compared to RNN. But, the improvement is only marginal. For VI-RNN, the model performance becomes better as λ is increased from 0.01 to 1. When λ becomes too large, the error of VI-RNN starts to increase. It is shown that at $\lambda = 10$ the errors of VI-RNN become larger than those of RNN. This is a typical behavior of a penalized maximum log likelihood, or a regularized optimization, method, in which the model performance starts to degrade when the regularization term becomes too large. For the one-step-ahead prediction task, although the error metrics of VI-RNN are smaller than RNN for a proper range of λ , the difference is within a range of statistical noise. This is due to the nature of a sequential inference problem; simply, when y_t is provided as a input, the prediction of y_{t+1} will not deviate too much.

Figure 2 shows the multiple-step forecasts from RNN and VI-RNN for two trajectories. The Monte Carlo simulations are performed with $N_s = 1,000$ samples. To initiate the RNN models, $\mathbf{Y}_{-200:0}$ is used. The advantages of the variational inference model are clearly shown in the multiple-step forecast tasks. Although RNN makes good predictions at a short forecast horizon, it quickly starts to deviate from the ground truth for $t > 100$. On the other hand, the multiple-step prediction of VI-RNN stays very close to the ground truth for the simulation horizon shown in figure 2. It is also shown that the model uncertainty, represented by the 95% prediction interval, of VI-RNN stays much tighter than that of RNN over the forecast horizon.

For a quantitative comparison, the temporal growth of a normalized mean absolute error (NMAE) and a normalized width of the 95% prediction interval (W_{95}) are shown in figure 3. The metrics are defined as

$$(3.8) \quad NMAE(t) = \frac{1}{N_{test}} \sum_{k=1}^{N_{test}} \frac{|E[y_t^k] - \phi^k(t\delta t)|}{std(\phi^k)},$$

$$(3.9) \quad W_{95}(t) = \frac{1}{N_{test}} \sum_{k=1}^{N_{test}} \frac{U_{95}(y_t^k) - L_{95}(y_t^k)}{std(\phi^k)}.$$

Here, N_{test} is the number of testing trajectories, $std(\phi)$ is the standard deviation of a trajectory ϕ , and U_{95} and L_{95} , respectively, denote the upper and lower bounds of the 95% prediction interval. Multiple-step forecasts are performed from five different initial conditions, $t_0 = (300, 350, 400, 450, 500)$, for the entire 100 trajectories in \mathcal{D}_V ,

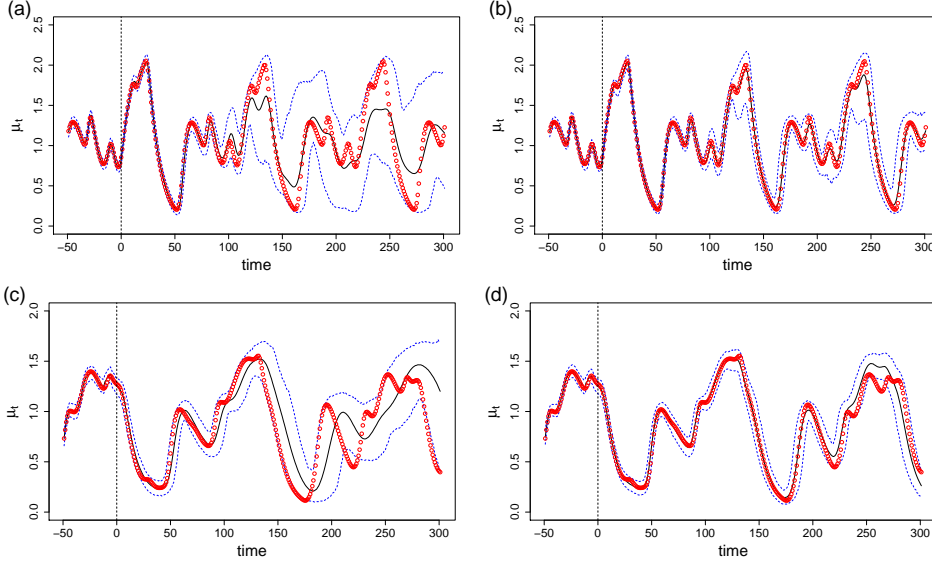


FIG. 2. Multiple-step forecast of the Mackey-Glass time series for two sets of the parameters, (α, γ, τ) ; (a,b) $(0.305, 0.092, 22.19)$, and (c,d) $(0.227, 0.098, 39.83)$. (a,c) are computed from RNN, and (b,d) are VI-RNN with $\lambda = 1$. The solid and dashed lines, respectively, denote the expectation and 95% prediction interval, and the circles (\circ) are the ground truth. The vertical dashed line denotes the starting point of the simulation.

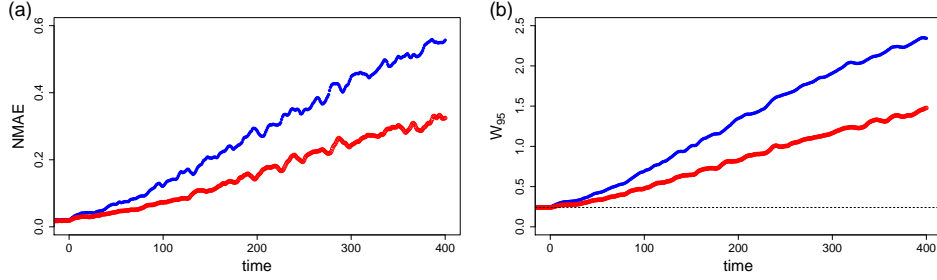


FIG. 3. Temporal growth of (a) normalized mean absolute errors and (b) widths of 95% prediction interval of RNN (\bullet) and VI-RNN trained with $\lambda = 1$ (\circ) for the multiple-step forecast. The dashed line in (b) denotes the noise level.

which makes $N_{test} = 500$. It is clearly shown that the multiple-step forecast of RNN shows much more rapid growth of NMAE and W_{95} than those of VI-RNN. At $t = 400$, NMAE of VI-RNN is only about 58% of RNN.

To have a better understanding on VI-RNN, the posterior distributions are computed from the training data, \mathcal{D}_T . The posterior distributions are computed at 5 different time stamps for the entire 400 trajectories in \mathcal{D}_T . Figure 4 shows absolute value of the correlation coefficients between the latent variables, *i.e.*, $|Cor(\mathbf{z}, \mathbf{z})|$, for four different penalty parameters, λ . The contribution of the Kullback-Leibler divergence to the loss function (2.25) increases linearly with λ , which pushes $q(\mathbf{z}|\mathbf{Y})$ towards the prior distribution, $p(\mathbf{z})$. Because $p(\mathbf{z})$ is given by an independent Gaussian distribution, it is shown that \mathbf{z} also becomes linearly independent from each other as λ increases.

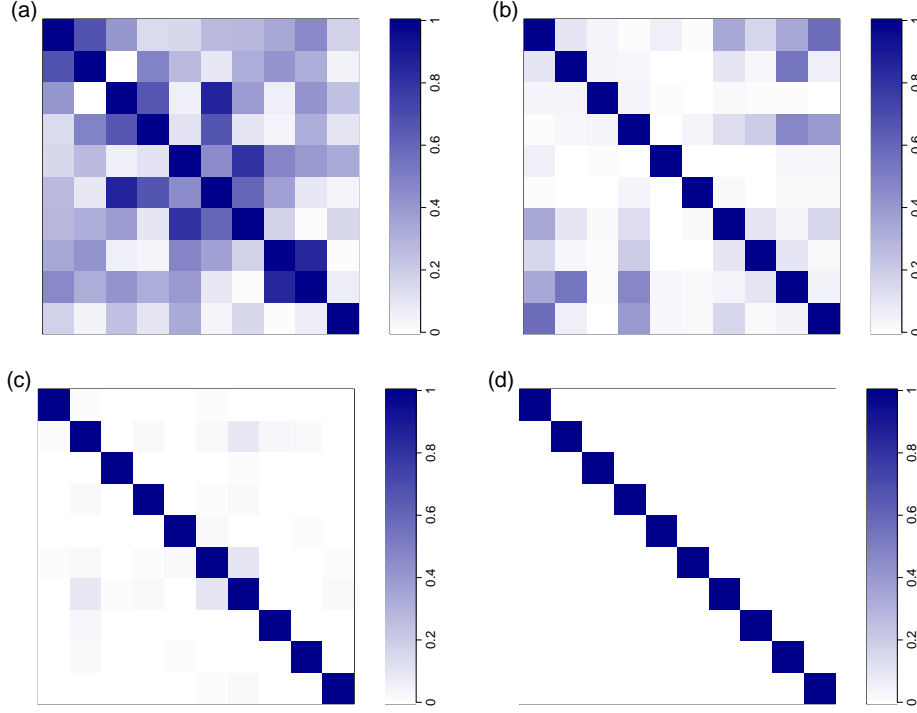


FIG. 4. Absolute value of correlation between \mathbf{z} for VI-RNN trained with (a) $\lambda = 0.01$, (b) $\lambda = 0.1$, and (c) $\lambda = 1.0$, and (d) $\lambda = 10.0$.

In the posterior distribution, the mean components (\mathbf{m}_q) contain information about the physical parameters, *e.g.*, (α, γ, τ) , while the standard deviation (σ_q) represents uncertainty around the estimation. To investigate the behavior of \mathbf{z} , a principal component analysis (PCA) is performed for \mathbf{m}_q . Figure 5 (a) shows the cumulative eigenvalues of the PCA components of \mathbf{m}_q ;

$$(3.10) \quad \zeta_i = \frac{\sum_{j=1}^i \nu_j}{\sum_{j=1}^{N_q} \nu_j},$$

in which ν_j is the j -th eigenvalue of PCA. The cumulative eigenvalue, ζ_i , indicates the fraction of variations in the data captured by the first i -th PCA modes. It is shown that, for the range of λ in this study, the first three modes can represent more than 90% of the variations in the data, *i.e.*, $\zeta_3 > 0.9$ for $0.01 \leq \lambda \leq 10$. Note that the Mackey-Glass time series has three random parameters. In particular, for $\lambda = 1$, ζ_3 becomes larger than 0.998, indicating the variations in the data can be almost completely explained by only the first three modes. When $\lambda = 10$, the posterior distribution becomes almost isotropic, which makes $\zeta_1 > 0.98$.

Figure 5 (b) shows an element-wise Kullback-Leibler divergence,

$$(3.11) \quad D_{KL_i} = \frac{1}{N_{test}} \sum_{k=1}^{N_{test}} \frac{1}{2} \left(\frac{m_{q_i}^{(k)2} + \sigma_{q_i}^{(k)2}}{\sigma_z^2} - 1 \right) - \log \frac{\sigma_{q_i}^{(k)}}{\sigma_z}.$$

Here, the standard deviation of the prior $p(\mathbf{z})$ is $\sigma_z = 1$. When $\lambda = 1$, the distributions

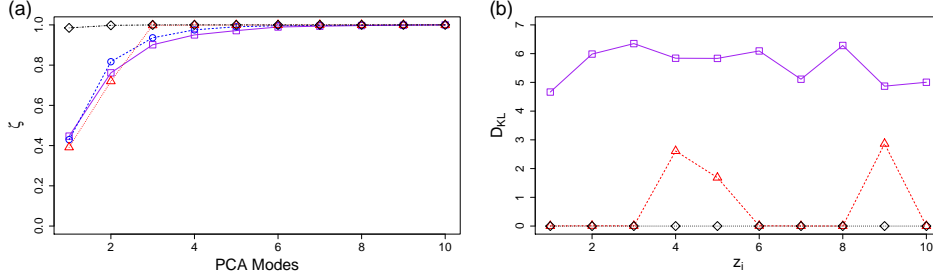


FIG. 5. (a) Cumulative eigenvalues of PCA modes of m_q for $\lambda = 0.01$ (\square), 0.1 (\circ), 1.0 (\triangle), and 10.0 (\diamond). (b) Element-wise Kullback-Leibler divergence for $\lambda = 0.01$ (\square), 1.0 (\triangle), and 10.0 (\diamond).

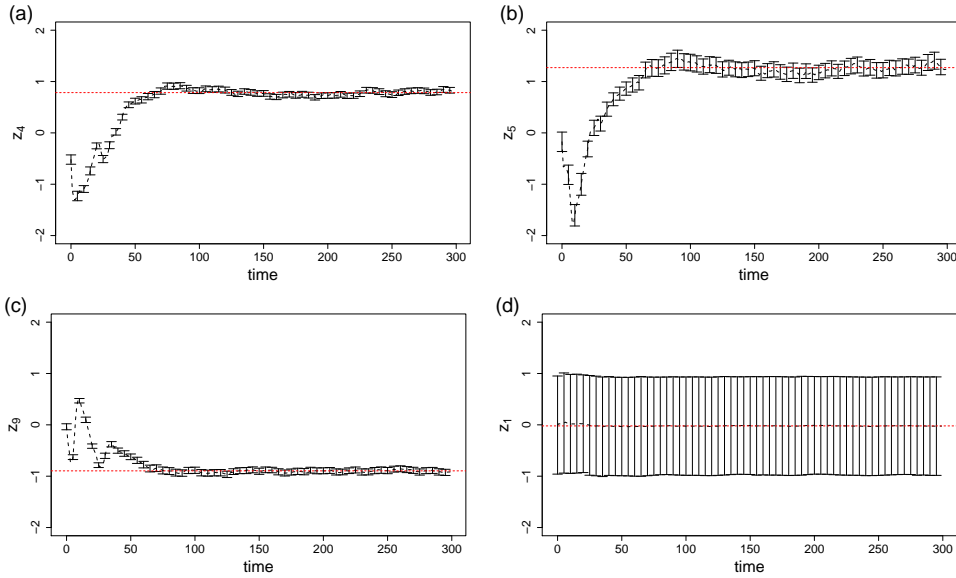


FIG. 6. The posterior distribution, $q(z_i|\mathbf{Y}_{0:t})$, as a function of t for a sample trajectory in \mathcal{D}_V . VI-RNN is trained with $\lambda = 1$; (a) z_4 , (b) z_5 , (c) z_9 , and (d) z_1 . The dashed line is m_q and σ_q is denoted as the error bars. The horizontal line is the time average of m_q over $t = 200 \sim 300$.

of only three elements of \mathbf{z} (z_4, z_5, z_9) become significantly different from $p(\mathbf{z})$. When $\lambda = 10$, $q(\mathbf{z}|\mathbf{Y})$ is almost equal to $p(\mathbf{z})$, *i.e.*, the latent variable becomes just a random noise.

A recurrent neural network models a stationary process. After a characteristic time scale, effects of an impulse vanishes and the internal state of an RNN recovers a stationary dynamics [44]. Considering this stationary nature of RNN, we employ a pre-trained RNN to provide the conditioning variable for $q(\mathbf{z}|\mathbf{Y}_{0:t})$. It is assumed that $q(\mathbf{z}|\mathbf{Y}_{0:t})$ will be invariant once t is larger than the characteristic timescale of the conditioning RNN. To test this assumption, in figure 6, $q(\mathbf{z}|\mathbf{Y}_{0:t})$ are computed for $t = 1, \dots, 300$;

$$(3.12) \quad \mathbf{h}_i^{pre} = \Psi_h^{pre}(\mathbf{y}_{i-1}, \mathbf{h}_{i-1}^{pre}),$$

$$(3.13) \quad \mathbf{z}_i \sim \hat{\boldsymbol{\eta}}(\mathbf{h}_i^{pre}), \text{ for } i = 1, \dots, 300.$$

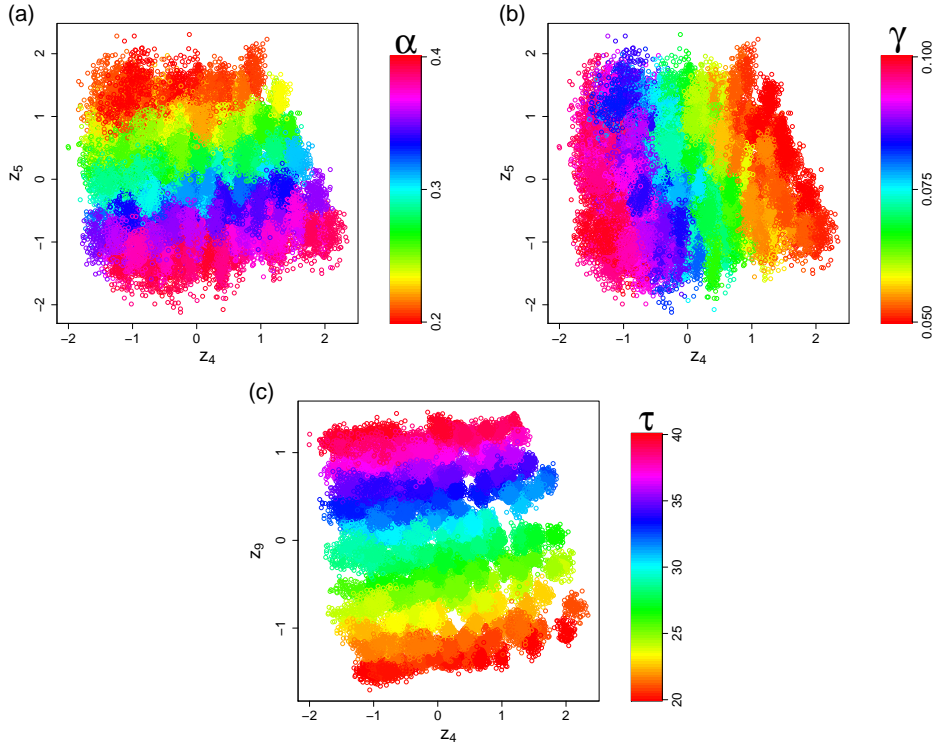


FIG. 7. The posterior distribution projected onto the three non-trivial dimensions; (a) $z_4 - z_5$, (b) $z_4 - z_5$, and (c) $z_4 - z_9$ planes. The symbols denote the samples from $q(\mathbf{z}|\mathbf{Y}^k)$ for all $\mathbf{Y}^k \in \mathcal{D}_T$. The symbols are color-coded with (a) α , (b) γ , and (c) τ values of the corresponding trajectory.

TABLE 2
Correlation between the latent variables and the random parameters

	α	γ	τ
z_4	0.28	0.93	-0.22
z_5	-0.95	-0.14	-0.04
z_9	-0.04	-0.12	0.98

In figure 6 (a-c), it is shown that indeed $q(\mathbf{z}|\mathbf{Y}_{0:t})$ converges to a stable distribution for $t > 100$. It is also shown that σ_q of the three non-trivial latent variables (z_4, z_5, z_9) are much smaller than the prior, σ_z . On the other hand, figure 6 (d) shows that the distributions of the other seven trivial latent variables follow that of the prior, $\mathcal{N}(0, 1)$, from the beginning and remain unchanged.

The results so far suggest that VI-RNN is capable of correctly identifying the dimensions of the random parameters from the data in an unsupervised way, *i.e.*, without giving any direct information about the dimensionality of the random parameters. To show a more direct evidence, in figure 7, we show \mathbf{z} projected onto the three non-trivial dimensions (z_4, z_5, z_9) and color-code with the random parameters. First, $q(\mathbf{z}|\mathbf{Y})$ are evaluated at five different time stamps for all 400 trajectories in \mathcal{D}_T . Then, 20 samples are drawn from the each $q(\mathbf{z}|\mathbf{Y})$. Those samples are plotted on the $z_4 - z_5$ and $z_4 - z_9$ planes, and color-coded with the values of (α, γ, τ) of

the corresponding trajectories. It is clearly shown that those three non-trivial latent variables indeed capture the variations of the random parameters without having any prior information about the complex nonlinear dynamical system. Table 2 shows the correlation between the random parameters and \mathbf{z} . It is shown that the correlation between a random parameter and the corresponding dimension of \mathbf{z} is larger than 0.9.

3.2. Forced Van der Pol Oscillator. For the next example, we consider a forced Van der Pol oscillator (VDP), which is given by the following equations,

$$(3.14) \quad \frac{d^2\phi(t)}{dt^2} - \gamma(1 - \phi^2(t))\frac{d\phi(t)}{dt} + \phi(t) + \alpha u(t) = 0.$$

An Ornstein-Uhlenbeck process is used as the exogenous forcing, $u(t)$,

$$(3.15) \quad du = -\theta u dt + u_{ref} \sqrt{2\theta} dW,$$

in which W is the Wiener process and the stationary standard deviation of $u(t)$ is $u_{ref} = 1$. The parameters in (3.14–3.15) are random variables,

$$(3.16) \quad \gamma \sim \mathcal{U}(1, 4), \quad \alpha \sim \mathcal{U}(0.25, 1), \quad \text{and} \quad \theta \sim \mathcal{U}(0.25, 1).$$

Now, the dataset, \mathcal{D} , consists of a tuple, $(\mathbf{Y}_{0:T}, \mathbf{U}_{0:T})$. Here, we are interested in an inference on \mathbf{Y} given \mathbf{U} . Hence, the random variable, θ , does not play a role in the inference. Because the forcing amplitude, α , is a random variable, the effects of $u(t)$ on the dynamics of VDP vary from one trajectory to another, which makes it a challenging inference problem. Figure 8 shows two sample trajectories of (\mathbf{Y}, \mathbf{U}) .

The equations of the forced VDP, (3.14 – 3.15), are numerically integrated by using a third-order Adams-Bashforth method with a time step size of 0.001, and a time series is generated by downsampling to make the sampling interval, $\delta = 0.2$. Then, a zero-mean Gaussian white noise is added as shown in (3.4). The standard deviation of the noise process is, $\sigma_\epsilon = 0.075$, which is about 5% of the standard deviation of $\mathbf{Y} \in \mathcal{D}$. Note that the noise is added only to \mathbf{Y} , not \mathbf{U} .

In figure 9, the multiple-step forecasts of RNN and VI-RNN are compared. VI-RNN is trained with $\lambda = 1$. In the multiple-step forecast, the exogenous forcing, \mathbf{u} , is given for the entire forecast horizon and the observation is given only up to $t = 0$, *i.e.*, the dataset consists of $(\mathbf{Y}_{-200:0}, \mathbf{U}_{-200:300})$. Similar to the Mackey-Glass time series, VI-RNN is able to make a much more accurate long-term forecast compared to RNN.

The multiple-step forecast accuracies and the uncertainty ranges are shown in figure 10. As expected, both NMAE and W_{95} of VI-RNN show much slower growths in time compared to those of RNN. In a short-range forecast, $t < 50\delta t$, the difference between VI-RNN and RNN is not noticeable. However, as the forecasting horizon, t , increases, the advantage of VI-RNN becomes more pronounced.

In [45], it is shown that a RNN, trained on one long trajectory, can make an accurate long-term forecast of VDP, where the prediction uncertainty remains stable even for 3000-step ahead forecasts. However, in this problem, the RNN is trained with an ensemble of trajectories with different parameters, which makes it difficult for the RNN to identify the dynamics of the trajectory. For $t = -200\delta t \sim 0$, the observations, y_t , are provided to constrain the behavior of the RNN. In the short-term forecast, $0 < t < 100\delta t$, the RNN simulates the dynamics close to what it learned from $\mathbf{Y}_{-200:0}$ due to an inertia. Eventually, the internal states of the RNN start to diverge, resulting in the increase in the prediction uncertainty. On the other hand, VI-RNN constrains the behavior of its decoder RNN around the one identified

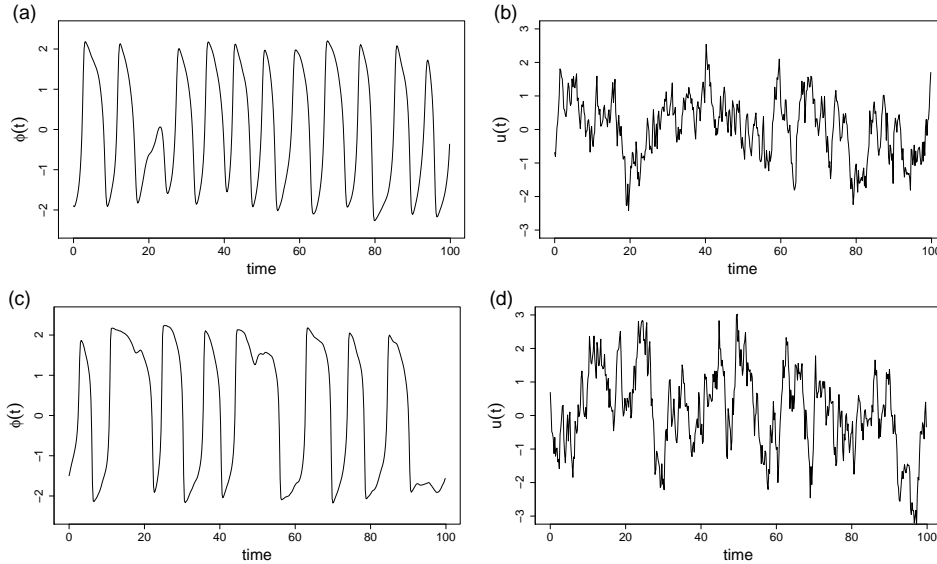


FIG. 8. Sample trajectories of the forced Van der Pol oscillator (a,c) and the corresponding exogenous forcing (b,d) for different sets of the parameters; (a) $(\alpha, \gamma) = (0.68, 1.77)$, (b) $\theta = 0.42$, (c) $(\alpha, \gamma) = (0.94, 3.63)$, (d) $\theta = 0.66$.

by $q(\mathbf{z}|\mathbf{Y}_{-200:0})$, which makes it possible to make a stable simulation for a much longer time horizon.

Figure 11 shows inferences from $q(\mathbf{z}|\mathbf{Y})$ for the training dataset, \mathcal{D}_T . It is shown in figure 11 (a) that the cumulative eigenvalues becomes larger than 0.99 from the second PCA modes, $\zeta_2 = 0.998$, indicating the variations in \mathbf{z} for \mathcal{D}_T can be almost totally explained with only two variables. In fact, figure 11 (b) shows that only two dimensions (z_8, z_{10}) are significantly different from the prior distribution.

The two meaningful dimensions of \mathbf{z} color-coded with the random parameters are shown in figure 12. Similar to the Mackey-Glass time series, the random parameters show almost linear variations in the $z_8 - z_{10}$ plane.

4. Summary. A deep learning approach is proposed to learn the dynamics from a time series dataset of a dynamical system with unknown parameters without any prior knowledge on the dynamical system or the dimensionality of the parameters. The learning problem is formulated as a variational inference problem, in which the effects of the parameters are approximated by introducing a latent variable, \mathbf{z} . In the variational inference framework, two artificial neural networks are jointly trained, one feedforward network to compute the approximate posterior distribution, $q(\mathbf{z}|\mathbf{Y})$, and a recurrent neural network to approximate the dynamics given the latent state, *e.g.*, $\mathbf{y}_{t+1} = \Psi^{VI}(\mathbf{y}_t, \mathbf{z})$. To make the inference model flexible, the conditioning variable for $q(\mathbf{z}|\mathbf{Y})$ is obtained from a pre-trained recurrent neural network, which is trained in a standard way without considering the randomness in the parameters. The loss function is derived from the evidence lower bound of the marginal data likelihood function. The loss function resembles a penalized maximum likelihood method, in which the Kullback-Leibler divergence acts as a penalization to impose a sparsity in \mathbf{z} , while the reconstruction error term provides the standard maximum likelihood estimator of a recurrent neural network. It is shown that due to the lack of a reference

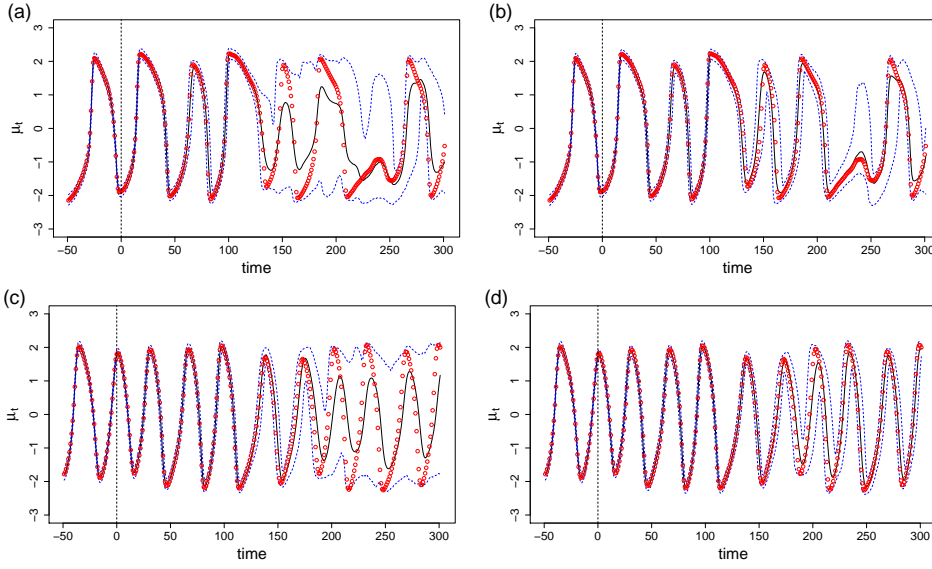


FIG. 9. Multiple-step forecast of the Van der Pol oscillator for two sets of the parameters, (α, γ) ; (a,b) $(0.668, 2.271)$, and (c,d) $(0.378, 1.035)$. (a,c) are computed from RNN, and (b,d) are from VI-RNN with $\lambda = 1$. The solid and dashed lines, respectively, denote the expectation and 95% prediction interval, and the circles (\circ) are the ground truth. The time is normalized by the sampling interval, δt . The vertical dashed line denotes the starting point of the multiple-step forecast.

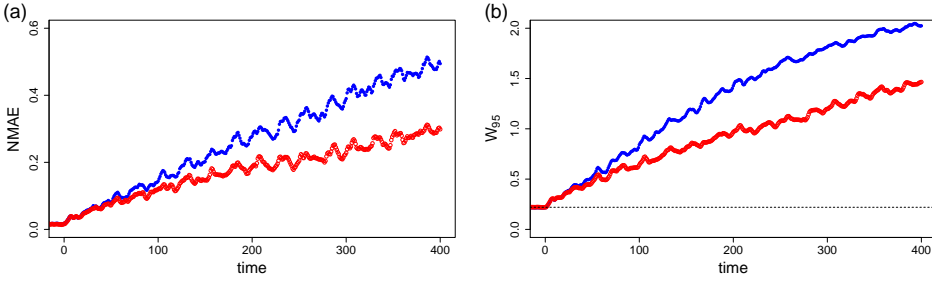


FIG. 10. Temporal growth of (a) normalized mean absolute error and (b) width of 95% prediction interval for RNN (\bullet) and VI-RNN (\circ) for the multiple-step forecast. The dashed line in (b) denotes the noise level. The time is normalized by the sampling interval, δt .

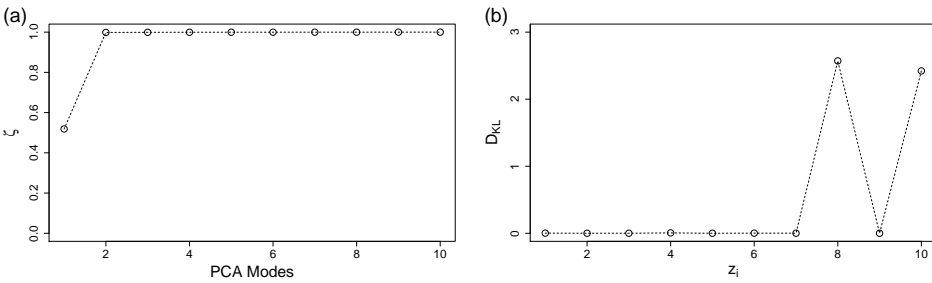


FIG. 11. (a) Cumulative eigenvalues of PCA modes of \mathbf{m}_q and (b) element-wise Kullback-Leibler divergence.

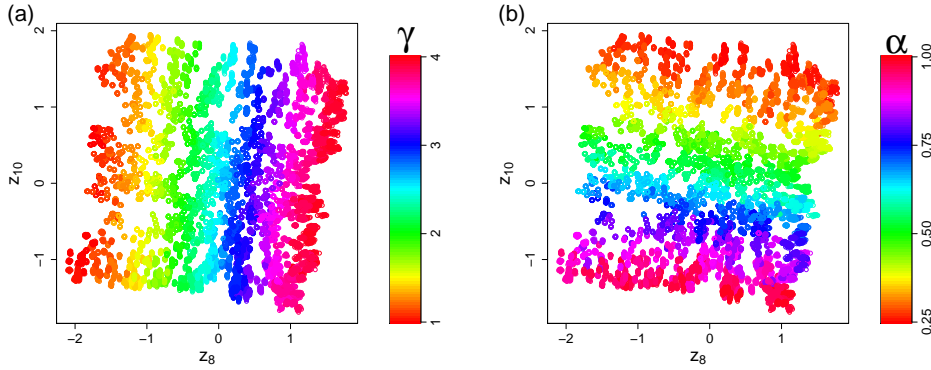


FIG. 12. The posterior distribution projected onto the two non-trivial dimensions; $z_8 - z_{10}$ plane. The symbols denote the samples from $q(\mathbf{z}|\mathbf{Y}^k)$ for all $\mathbf{Y}^k \in \mathcal{D}_T$. The color coding denotes (a) γ and (b) α .

point, the loss function can be rescaled, introducing a penalty parameter, λ . The penalty parameter controls the relative contribution between the Kullback-Leibler divergence and the reconstruction error terms to the loss function.

The proposed variational-inference model, VI-RNN, is tested by using two nonlinear dynamical systems with random parameters. It is shown that, although VI-RNN does not show advantages over RNN in a simple one-step prediction task, VI-RNN outperforms RNN in the multiple-step predictions as the prediction horizon increases. In the beginning of the stochastic simulation, the RNN prediction shows a good agreement with the ground truth due to an inertia developed in the spin-up period. However, as the simulation time increases, the effects of the inertia vanishes and the RNN prediction quickly diverges from the ground truth, which is accompanied by a rapid increase in the prediction uncertainty. On the other hand, VI-RNN first makes an inference about the effects of the unknown parameters from the data in the spin-up period and use the outcome to drive the simulation. Hence, VI-RNN proves a much more stable and accurate simulation compared to RNN.

In the numerical experiments, we keep the structures of the recurrent neural network used for VI-RNN and the standard RNN approaches exactly the same, except for the input dimensions. The input variable of VI-RNN is appended with the latent state, \mathbf{z} . Hence, any improvement of VI-RNN over RNN can be attributed to how well the approximate posterior, $q(\mathbf{z}|\mathbf{Y})$, represents the effects of random parameters. It is shown that VI-RNN is capable of identifying the dimensionality of the random parameters and each meaningful dimension of \mathbf{z} has a direct correspondence to one of the random parameters. The penalty parameter, λ , plays a role in the inference of VI-RNN. Increasing λ makes $q(\mathbf{z}|\mathbf{Y})$ be similar to the prior distribution. Because an independent Gaussian distribution is used as the prior distribution, a large λ makes \mathbf{z} linearly independent. Since it was empirically shown that a large value of the penalty parameter, $\lambda \gg 1$, results in a better inference in [21], many of the follow-up studies adopt the suggestion. However, as shown in our derivation, the loss function does not have a reference scale, and it also depends on a few parameters, such as the dimensions of \mathbf{y}_t and \mathbf{z} , and the length of the training sequence. Hence, it is difficult to assert what is the proper range of λ . From the numerical experiments, we suggest to use a

small λ , which makes \mathbf{z} almost linearly independent, *e.g.*,

$$\lambda^* = \min \lambda \quad \text{s.t.} \quad \|Cor(\mathbf{z}, \mathbf{z}) - \mathbf{I}\|_{max} < \delta,$$

where the tolerance level, δ , may be chosen to be 0.1 or smaller. Note that, however, the numerical experiments suggest that the results are not highly sensitive to λ . Even though \mathbf{z} becomes linearly dependent at a small λ , a principal component analysis of \mathbf{z} can be used to identify an effective dimension of the problem.

In the present study, we focus only on a stationary process, in which the unknown parameters do not change over time. We expect the present method can be applied to identify a quasi-steady process, where the temporal changes of the parameters occur at a much longer timescale than the time required to identify the latent state (see figure 6). It is a subject of a follow-up study to expand the proposed framework to make a robust inference on the dynamical systems with time-varying random parameters.

Appendix A. Joint optimization of prior and posterior.

The negative evidence lower bound (ELBO) of a VI problem is

$$(A.1) \quad \mathcal{L} = D_{KL}(q(\mathbf{z}|\mathbf{X})||p(\mathbf{z})) - E_{\mathbf{z} \sim q(\mathbf{z}|\mathbf{X})}[\log p(\mathbf{X}|\mathbf{z})],$$

in which \mathbf{X} is the data, $p(\mathbf{z})$ is a prior distribution, and $q(\mathbf{z}|\mathbf{X})$ is the approximate posterior distribution. Let assume that the prior distribution, $p(\mathbf{z})$, is a Gaussian distribution with a diagonal covariance,

$$p(\mathbf{z}) = \mathcal{N}(\mathbf{z}; \mathbf{m}_0, \text{diag}(\gamma_0)),$$

and similarly the approximate posterior distribution is

$$q(\mathbf{z}|\mathbf{X}) = \mathcal{N}(\mathbf{z}; \mathbf{m}_q, \text{diag}(\gamma_q)).$$

Here, γ_0 and γ_q denote the variances of the respective Gaussian distributions. We use an artificial neural network ($\boldsymbol{\eta}$) to approximate the posterior distribution, such that

$$(A.2) \quad (\mathbf{m}_q, \gamma_q) = \boldsymbol{\eta}(\mathbf{X}).$$

Following the formulation of [9], let assume that the prior distribution is computed from another artificial neural network,

$$(A.3) \quad (\mathbf{m}_0, \gamma_0) = \boldsymbol{\zeta}(\mathbf{X}).$$

Without loss of generality, we assume $N_z = 1$. Then, the Kullback-Leibler divergence in (2.9) can be written as

$$(A.4) \quad D_{KL}(q(\mathbf{z}|\mathbf{X})||p(\mathbf{z})) = \frac{1}{2} \left\{ \frac{\gamma_q + (m_0 - m_q)^2}{\gamma_0} - \log \left(\frac{\gamma_q}{\gamma_0} \right) \right\} - \frac{1}{2}.$$

At a (local) minimum of \mathcal{L} , the following condition holds

$$(A.5) \quad \nabla_{\boldsymbol{\theta}} \mathcal{L} = \mathbf{0},$$

in which $\boldsymbol{\theta} = (m_0, m_q, \gamma_0, \gamma_q)$. The gradients with respect to $\boldsymbol{\theta}$ are

$$(A.6) \quad \frac{\partial \mathcal{L}}{\partial m_0} = \frac{1}{\gamma_0} (m_0 - m_q) = 0,$$

$$(A.7) \quad \frac{\partial \mathcal{L}}{\partial \gamma_0} = -\frac{1}{2\gamma_0^2} [\gamma_q + (m_0 - m_q)^2] + \frac{1}{2\gamma_0} = 0,$$

$$(A.8) \quad \frac{\partial \mathcal{L}}{\partial m_q} = \frac{1}{2\gamma_0} (m_q - m_0) - \beta = 0,$$

$$(A.9) \quad \frac{\partial \mathcal{L}}{\partial \gamma_q} = \frac{1}{2\gamma_0} - \frac{1}{2\gamma_q} - \alpha = 0,$$

in which

$$\alpha = \frac{\partial}{\partial \gamma_q} E_{z \sim q(z|\mathbf{X})} [\log p(\mathbf{X}|z)], \quad \text{and} \quad \beta = \frac{\partial}{\partial m_q} E_{z \sim q(z|\mathbf{X})} [\log p(\mathbf{X}|z)].$$

Hence, at a minimum, the solution should satisfy

$$(A.10) \quad m_0 - m_q = 0,$$

$$(A.11) \quad (\gamma_0 - \gamma_q) - (m_0 - m_q)^2 = 0,$$

$$(A.12) \quad (m_q - m_0) - 2\beta\gamma_0 = 0,$$

$$(A.13) \quad (\gamma_q - \gamma_0) - 2\alpha\gamma_0\gamma_q = 0,$$

which results in a trivial solution,

$$m_0 = m_q, \quad \gamma_0 = \gamma_q, \quad \alpha = 0, \quad \beta = 0.$$

Because both (m_0, γ_0) and (m_q, γ_q) are unknown variables, *i.e.*, outputs of artificial neural networks, the probabilistic model is unidentifiable. It is also important to note that the formulation leads to

$$(A.14) \quad \frac{\partial}{\partial z} E_{z \sim q(z|\mathbf{X})} [\log p(\mathbf{X}|z)] = 0,$$

which implies that the reconstruction error is not dependent on the latent variable. In other words, the latent variable does not play a role in the inference.

Appendix B. Training of VI-RNN. Let $\boldsymbol{\theta}_\eta$ and $\boldsymbol{\theta}_\Psi$ be the parameters of η and Ψ , respectively. In the model training, we aim to find the parameters, which minimize the loss function by solving the following optimization problem,

$$(B.1) \quad \min_{\boldsymbol{\theta}_\eta, \boldsymbol{\theta}_\Psi} \sum_{k=1}^K \lambda \mathcal{L}_q^k + \mathcal{L}_y^k.$$

It is typical to use a variant of Stochastic Gradient Descent (SGD) methods to solve (B.1). Using a SGD, the parameters are updated as

$$(B.2) \quad \begin{bmatrix} \boldsymbol{\theta}_\eta^{n+1} \\ \boldsymbol{\theta}_\Psi^{n+1} \end{bmatrix} = \begin{bmatrix} \boldsymbol{\theta}_\eta^n \\ \boldsymbol{\theta}_\Psi^n \end{bmatrix} - \xi \begin{bmatrix} \nabla_{\boldsymbol{\theta}_\eta^n} (\lambda \mathcal{L}_q^{s_n} + \mathcal{L}_y^{s_n}) \\ \nabla_{\boldsymbol{\theta}_\Psi^n} \mathcal{L}_y^{s_n} \end{bmatrix}, \quad \text{for } n = 1, \dots, N_{max},$$

in which n is the iteration count, N_{max} is the maximum number of iterations, ξ is a learning rate, and $s_n \sim \mathcal{U}(\mathcal{D})$ is a uniform random variable in \mathcal{D} to sample a trajectory

at each iteration. For now, we consider $N_z = d = 1$ for simplicity. Note that, due to the diagonal covariance assumptions for the inference and generative models, it is trivial to extend the results for a higher dimensional problem.

Computing the gradients of \mathcal{L}_q is straightforward;

$$(B.3) \quad \frac{\partial \mathcal{L}_q}{\partial \boldsymbol{\theta}_\eta} = \frac{\partial \mathcal{L}_q}{\partial m_q} \frac{\partial m_q}{\partial \boldsymbol{\theta}_\eta} + \frac{\partial \mathcal{L}_q}{\partial \log \sigma_q} \frac{\partial \log \sigma_q}{\partial \boldsymbol{\theta}_\eta}.$$

Here,

$$\frac{\partial \mathcal{L}_q}{\partial m_q} = \frac{m_q}{\sigma_z^2}, \quad \text{and} \quad \frac{\partial \mathcal{L}_q}{\partial \log \sigma_q} = \frac{\sigma_q^2}{\sigma_z^2} - 1.$$

The gradients of m_q and σ_q with respect to $\boldsymbol{\theta}_\eta$ can be easily computed by using a back propagation method on the computation of $\boldsymbol{\eta}$.

The loss function, \mathcal{L}_y , involves an expectation over \mathbf{z} , which is approximated by a Monte Carlo sampling

$$(B.4) \quad \mathcal{L}_y = -E_{z \sim q(z|\mathbf{Y}_{0:T})} \left[\sum_{t=1}^T \log p(y_t | \mathbf{h}_t) \right] \simeq -\frac{1}{M} \sum_{m=1}^M \left\{ \sum_{t=1}^T \log p(y_t | \mathbf{h}_t) \right\} \Big|_{z^m}.$$

Here, z^m is sampled from the posterior distribution, $q(z|\mathbf{Y}_{0:T})$, as

$$(B.5) \quad z^m = \mu_q + \sigma_q \epsilon^m, \quad \text{for } l = 1, \dots, M,$$

in which $\epsilon^m \sim \mathcal{N}(0, 1)$. Let define

$$l_t^m = -\log p(y_t | \mathbf{h}_t) \Big|_{z^m} = \left(\frac{1}{2} \frac{(y_t - \mu_t)^2}{\sigma_t^2} + \log \sigma_t \right) \Big|_{z^m}.$$

Note that the constant term is neglected. The SGD update requires to compute

$$(B.6) \quad \frac{\partial l_t^m}{\partial \boldsymbol{\theta}_\eta} = \frac{\partial l_t^m}{\partial z} \left(\frac{\partial z}{\partial m_q} \frac{\partial m_q}{\partial \boldsymbol{\theta}_\eta} + \frac{\partial z}{\partial \log \sigma_q} \frac{\partial \log \sigma_q}{\partial \boldsymbol{\theta}_\eta} \right) \Big|_{z^m}.$$

The gradient of l_t^m with respect to the latent variable is

$$(B.7) \quad \frac{\partial l_t^m}{\partial z} = \frac{\partial l_t^m}{\partial \mu_t} \frac{\partial \mu_t}{\partial z} + \frac{\partial l_t^m}{\partial \log \sigma_t} \frac{\partial \log \sigma_t}{\partial z},$$

where

$$\frac{\partial l_t^m}{\partial \mu_t} = \frac{\mu_t - y_t}{\sigma_t^2} \Big|_{z^m} \quad \text{and} \quad \frac{\partial l_t^m}{\partial \log \sigma_t} = 1 - \frac{(\mu_t - y_t)^2}{\sigma_t^2} \Big|_{z^m}.$$

A back propagation algorithm can be used to evaluate the gradients, $\frac{\partial \mu_t}{\partial z} \Big|_{z^m}$ and $\frac{\partial \log \sigma_t}{\partial z} \Big|_{z^m}$, in (B.7). From the random sampling procedure (B.5), it is clear that

$$(B.8) \quad \frac{\partial z}{\partial m_q} \Big|_{z^m} = 1, \quad \text{and} \quad \frac{\partial z}{\partial \log \sigma_q} \Big|_{z^m} = \sigma_q \epsilon^m.$$

Now, the gradient of \mathcal{L}_y with respect to $\boldsymbol{\theta}_\eta$ can be computed as

$$(B.9) \quad \nabla_{\boldsymbol{\theta}_\eta} \mathcal{L}_y = \left[\frac{1}{M} \sum_{m=1}^M \sum_{t=1}^T \frac{\partial l_t^m}{\partial z} \right] \frac{\partial m_q}{\partial \boldsymbol{\theta}_\eta} + \left[\frac{\sigma_q}{M} \sum_{m=1}^M \left(\epsilon^m \sum_{t=1}^T \frac{\partial l_t^m}{\partial z} \right) \right] \frac{\partial \log \sigma_q}{\partial \boldsymbol{\theta}_\eta}.$$

Here, the gradients of m_q and σ_q with respect to $\boldsymbol{\theta}_\eta$ can be easily computed by using a back propagation method on the computation of $\boldsymbol{\eta}$.

In summary, the gradients of the loss function are,

$$(B.10) \quad \frac{\partial \mathcal{L}}{\partial \boldsymbol{\theta}_\eta} = \left[\lambda \frac{m_q}{\sigma_z^2} + \frac{1}{M} \sum_{m=1}^M \sum_{t=1}^T \frac{\partial l_t^m}{\partial z} \right] \frac{\partial m_q}{\partial \boldsymbol{\theta}_\eta} + \left[\lambda \left(\frac{\sigma_q^2}{\sigma_z^2} - 1 \right) + \frac{\sigma_q}{M} \sum_{m=1}^M \left(\epsilon^m \sum_{t=1}^T \frac{\partial l_t^m}{\partial z} \right) \right] \frac{\partial \log \sigma_q}{\partial \boldsymbol{\theta}_\eta},$$

$$(B.11) \quad \frac{\partial \mathcal{L}}{\partial \boldsymbol{\theta}_\Psi} = \frac{1}{M} \sum_{m=1}^M \left[\sum_{t=1}^T \left(\frac{\mu_t - y_t}{\sigma_t^2} \right) \frac{\partial \mu_t}{\partial \boldsymbol{\theta}_\Psi} + \left(1 - \frac{(\mu_t - y_t)^2}{\sigma_t^2} \right) \frac{\partial \log \sigma_t}{\partial \boldsymbol{\theta}_\Psi} \right]_{z^m}.$$

For each SGD iteration, first (m_q, σ_q) are computed from the training trajectory $(\mathbf{Y}_{0:T})$, and M samples are drawn from $q(z|\mathbf{Y}_{0:T})$ as shown in (B.5). Then, the RNN simulations are performed forward in time for the samples,

$$(B.12) \quad (\mu_t, \log \sigma_t)|_{z^m} = \boldsymbol{\Psi}(y_{t-1}, \mathbf{h}_{t-1}, z^m), \text{ for } t = 1, \dots, T \ \& \ m = 1, \dots, M.$$

Finally, the gradients of the loss function are computed by (B.10–B.11) through a back-propagation algorithm and the parameters of the artificial neural networks are updated by (B.3).

Appendix C. Monte Carlo simulation of VI-RNN.

Algorithm C.1 Monte Carlo simulation of VI-RNN

Input: Data $(\mathbf{Y}_{-t:0}, \mathbf{U}_{-t:0})$, MC sample size (N_s) , forecast horizon (T_f)

Output: N_s samples from $p(\mathbf{y}_i|\mathbf{Y}_{-t:0}, \mathbf{U}_{-t:i-1})$ for $i = 1, \dots, T_f$.

1. Compute the approximate posterior distribution:

Sequential update of $\boldsymbol{\Psi}^{pre}$ for $(\mathbf{Y}_{-t:0}, \mathbf{U}_{-t:0})$.

$$\mathbf{h}_i^{pre} = \boldsymbol{\Psi}_h^{pre}(\mathbf{y}_{i-1}, \mathbf{u}_{i-1}, \mathbf{h}_{i-1}^{pre}) \text{ for } i = -t + 1, \dots, 1.$$

Compute the approximate posterior distribution

$$(\mathbf{m}_q, \boldsymbol{\sigma}_q) = \hat{\boldsymbol{\eta}}(\mathbf{h}_0^{pre})$$

Draw N_s samples from $q(\mathbf{z}|\mathbf{Y}_{-t:0}, \mathbf{U}_{-t:0})$

$$\mathbf{z}^{(j)} = \mathbf{m}_q + \boldsymbol{\sigma}_q \odot \boldsymbol{\epsilon} \text{ for } j = 1, \dots, N_s, \text{ where } \boldsymbol{\epsilon} \sim \mathcal{N}(0, \mathbf{I}).$$

2. Simulate the decoder RNN with the input data $(\mathbf{Y}_{-t:0}, \mathbf{U}_{-t:0})$:

$$\mathbf{h}_i^{(j)} = \boldsymbol{\Psi}_h^{VI}(\mathbf{y}_{i-1}, \mathbf{u}_{i-1}, \mathbf{h}_{i-1}^{(j)}, \mathbf{z}^{(j)}).$$

for $i = -t + 1, \dots, 1$ and $j = 1, \dots, N_s$.

3. Monte Carlo simulation with the decoder RNN:

for $i = 1, T_s$ **do**

for $j = 1, N_s$ **do**

$$\text{Distribution of } \mathbf{y}_i: (\boldsymbol{\mu}_i^{(j)}, \boldsymbol{\sigma}_i^{(j)}) = \boldsymbol{\Psi}_y^{VI}(\mathbf{h}_i^{(j)})$$

$$\text{MC Sampling of } \mathbf{y}_i: \mathbf{y}_i^{(j)} = \boldsymbol{\mu}_i^{(j)} + \boldsymbol{\sigma}_i^{(j)} \odot \boldsymbol{\epsilon}$$

$$\text{Update RNN: } \mathbf{h}_{i+1}^{(j)} = \boldsymbol{\Psi}_h^{VI}(\mathbf{y}_i^{(j)}, \mathbf{h}_i^{(j)}, \mathbf{z}^{(j)}, \mathbf{u}_i).$$

end for

end for

- [1] M. S. ARULAMPALAM, S. MASKELL, N. GORDON, AND T. CLAPP, *A tutorial on particle filters for online nonlinear/non-gaussian bayesian tracking*, IEEE Trans. Signal Process., 50 (2002), pp. 174–188.
- [2] Y. BENGIO, A. COURVILLE, AND P. VINCENT, *Representation learning: A review and new perspectives*, IEEE Trans. Pattern Anal. Mach. Intell., 35 (2013), pp. 1798–1828.
- [3] C. M. BISHOP, *Pattern Recognition and Machine Learning*, Springer, 2006.
- [4] D. M. BLEI, A. KUCUKELBIR, AND J. D. MCAULIFFE, *Variational inference: A review for statisticians*, J. Am. Stat. Assoc., 112 (2017), pp. 859–877.
- [5] G. E. P. BOX, G. M. JENKINS, AND G. C. REINSEL, *Time series analysis*, John Wiley & Sons, Inc., 2008.
- [6] S. L. BRUNTON, B. R. NOACK, AND P. KOUMOUTSAKOS, *Machine learning for fluid mechanics*, Ann. Rev. Fluid Mech., 52 (2020), pp. 477–508.
- [7] S. L. BRUNTON, J. L. PROCTOR, AND J. N. KUTZ, *Discovering governing equations from data by sparse identification of nonlinear dynamical systems*, Proc. Natl. Acad. Sci., 113 (2016), pp. 3932 – 3937.
- [8] K. CHO, B. VAN MERRIENBOER, C. GULCEHRE, F. BOUGARES, H. SCHWENK, AND Y. BENGIO, *Learning phrase representations using rnn encoder-decoder for statistical machine translation*, in Proc. Conf. Empir. Methods Nat. Lang. Process., 2014.
- [9] J. CHUNG, K. KASTNER, L. DINH, K. GOEL, A. C. C, AND Y. BENGIO, *A recurrent latent variable model for sequential data*, in Adv. Neural Inf. Process. Syst., 2015, pp. 2980–2988.
- [10] T. ERNEUX, J. JAVALOYES, M. WOLFRUM, AND S. YANCHUK, *Introduction to focus issue: Time-delay dynamics*, Chaos, 27 (2017), p. 114201.
- [11] G. EVENSEN, *The ensemble Kalman filter: theoretical formulation and practical implementation*, Ocean Dyn., 53 (2003), pp. 343 – 367.
- [12] J. D. FARMER, *Chaotic attractors of an infinite-dimensional dynamical system*, Physica D, 4 (1982), pp. 366–393.
- [13] J. D. A. FERRANDIS, M. TRIANTAFYLLOU, C. CHRYSSOSTOMIDIS, AND G. E. KARNIADAKIS, *Learning functionals via LSTM neural networks for predicting vessel dynamics in extreme sea states*, ArXiv e-prints, (2019). <http://arxiv.org/abs/1912.13382>.
- [14] M. FRANGOS, Y. MARZOUK, K. WILLCOX, AND B. VAN BLOEMEN WAANDERS, *Surrogate and Reduced-Order Modeling: A Comparison of Approaches for Large-Scale Statistical Inverse Problems*, John Wiley & Sons, Ltd, 2010, ch. 7, pp. 123–149.
- [15] C. FURUSAWA AND K. KANEKO, *A dynamical-systems view of stem cell biology*, Science, 338 (2012), pp. 215–217.
- [16] N. GENEVA AND N. ZABARAS, *Modeling the dynamics of PDE systems with physics-constrained deep auto-regressive networks*, J. Comput. Phys., 403 (2020), p. 109056.
- [17] I. GOODFELLOW, Y. BENGIO, AND A. COURVILLE, *Deep Learning*, MIT Press, 2016. <http://www.deeplearningbook.org>.
- [18] F. HAMILTON, T. BERRY, AND T. SAUER, *Predicting chaotic time series with a partial model*, Phys. Rev. E, 92 (2015), p. 010902(R).
- [19] ———, *Ensemble Kalman filtering without a model*, Phys. Rev. X, 6 (2016), p. 011021.
- [20] A. C. HARVEY, *Forecasting, structural time series models and the Kalman filter*, Cambridge university press, 1990.
- [21] I. HIGGINS, L. MATTHEY, A. PAL, C. BURGESS, X. GLOROT, M. BOTVINICK, S. MOHAMED, AND A. LERCHNER, *β -vae: Learning basic visual concepts with a constrained variational framework*, in Proc. 5th Int. Conf. Learn. Represent., 2017.
- [22] W.-N. HSU, Y. ZHANG, AND J. GLASS, *Unsupervised learning of disentangled and interpretable representations from sequential data*, in Adv. Neural Inf. Process. Syst., 2017, pp. 1878–1889.
- [23] D. P. KINGMA AND J. L. BA, *ADAM: A method for stochastic optimization*, in Proc. 3rd Int. Conf. Learn. Represent., 2015. <http://arxiv.org/abs/1412.6980>.
- [24] D. P. KINGMA AND M. WELING, *Auto-encoding variational Bayes*, in Proc. 2nd Int. Conf. Learn. Represent., 2014. <http://arxiv.org/abs/1312.6114>.
- [25] E. N. LORENZ, *Deterministic Nonperiodic Flow.*, J. Atmos. Sci., 20 (1963), pp. 130–148.
- [26] I. LOSHCILOV AND F. HUTTER, *SGDR: Stochastic gradient descent with warm restarts*, in 5th Int. Conf. Learn. Represent., 2017.
- [27] B. LUSCH, J. N. KUTZ, AND S. L. BRUNTON, *Deep learning for universal linear embeddings of nonlinear dynamics*, Nature Comm., 9 (2018), p. 4950.
- [28] M. MACKEY AND L. GLASS, *Oscillation and chaos in physiological control systems*, Science, 197 (1977), pp. 287–289.
- [29] H. N. NAJM, *Uncertainty quantification and polynomial chaos techniques in computational fluid dynamics*, Ann. Rev. Fluid Mech., 41 (2009), pp. 35–52.

- [30] M. RAISSI, P. PERDIKARIS, AND G. KARNIADAKIS, *Physics-informed neural networks: A deep learning framework for solving forward and inverse problems involving nonlinear partial differential equations*, J. Comput. Phys., 378 (2019), pp. 686 – 707.
- [31] M. RAISSI, A. YAZDANI, AND G. E. KARNIADAKIS, *Hidden fluid mechanics: Learning velocity and pressure fields from flow visualizations*, Science, (2020).
- [32] J. O. RAMSAY, G. HOOKER, D. CAMPBELL, AND J. CAO, *Parameter estimation for differential equations: a generalized smoothing approach*, J. R. Statis. Soc. B, 69 (2007), pp. 741–796.
- [33] S. H. RUDY, J. N. KUTZ, AND S. L. BRUNTON, *Deep learning of dynamics and signal-noise decomposition with time-stepping constraints*, J. Comput. Phys., 396 (2019), pp. 483 – 506.
- [34] J. C. SPROTT, *Chaos and time-series analysis*, Oxford Univ. Press, Oxford, 2003.
- [35] J. C. SPROTT, *Elegant Chaos: Algebraically Simple Chaotic Flows*, World Scientific, 2010.
- [36] S. STROGATZ, *Nonlinear Dynamics And Chaos: With Applications To Physics, Biology, Chemistry, And Engineering (Studies in Nonlinearity)*, Westview Press, 2001.
- [37] G. SUGIHARA, R. MAY, H. YE, C.-H. HSIEH, E. DEYLE, M. FOGARTY, AND S. MUNCH, *Detecting causality in complex ecosystems*, Science, 338 (2012), pp. 496–500.
- [38] L. SUN, H. GAO, S. PAN, AND J.-X. WANG, *Surrogate modeling for fluid flows based on physics-constrained deep learning without simulation data*, Comput. Methods Appl. Mech. Engng., 361 (2020), p. 112732.
- [39] T. TÉL, A. DE MOURA, C. GREBOGI, AND G. KÁROLYI, *Chemical and biological activity in open flows: A dynamical system approach*, Phys. Rep., 413 (2005), pp. 91 – 196.
- [40] J. H. TU, C. W. ROWLEY, D. M. LUCHTENBURG, S. L. BRUNTON, AND J. N. KUTZ, *On dynamic mode decomposition: Theory and applications*, J. Comput. Dyn., 1 (2014), p. 391.
- [41] A. C. VENTURA, L. BRUNO, AND S. P. DAWSON, *Simple data-driven models of intracellular calcium dynamics with predictive power*, Phys. Rev. E, 74 (2006), p. 011917.
- [42] D. XIU AND G. KARNIADAKIS, *The Wiener-Askey polynomial chaos for stochastic differential equations*, SIAM J. Sci. Comput., 24 (2002), pp. 619–644.
- [43] Y. YANG AND P. PERDIKARIS, *Adversarial uncertainty quantification in physics-informed neural networks*, J. Comput. Phys., 394 (2019), pp. 136 – 152.
- [44] K. YEO, *Short note on the behavior of recurrent neural network for noisy dynamical system*, ArXiv e-prints,, (2019). <http://arxiv.org/abs/1904.05158>.
- [45] K. YEO AND I. MELNYK, *Deep learning algorithm for data-driven simulation of noisy dynamical system*, J. Comput. Phys., 376 (2019), pp. 1212 – 1231.
- [46] L. YINGZHEN AND S. MANDT, *Disentangled sequential autoencoder*, in Proc. 35th Int. Conf. Mach. Learn., vol. 80, 2018, pp. 5670–5679.
- [47] Y. ZHU AND N. ZABARAS, *Bayesian deep convolutional encoderdecoder networks for surrogate modeling and uncertainty quantification*, J. Comput. Phys., 366 (2018), pp. 415 – 447.